SPECTROSCOPIC INVESTIGATION OF PREMIXED $H_2/NH_3/N_2$-AIR FLAMES STABILIZED ON A H_2-AIR PILOT FLAME

A Thesis

by

KRISTI NALENE NAUDE

Submitted to the Graduate and Professional School of
Texas A&M University
in partial fulfillment of the requirements for the degree of

MASTER OF SCIENCE

Chair of Committee,	Waruna Kulatilaka
Committee Members,	Timothy Jacobs
	Lesley Wright
Head of Department,	Guillermo Aguilar

May 2023

Major Subject: Mechanical Engineering

ABSTRACT

Given that burning conventional hydrocarbon fuels produces harmful carbon-based emissions contributing to global warming, recent environmental initiatives have focused on removing carbon-based fuels from the transportation, power generation and industrial sectors. Although eliminating all combustion devices are not immediately feasible, carbon-free alternative fuels provide a potential intermediate solution. Ammonia (NH_3) is one such alternative, being relatively easy to store and transport in the liquid state, as well as having the ability to be produced from renewable sources without environmental damage. NH_3 is usually mixed with other fuels to form combustible blends due to its lower flame speed and instability during combustion. The fuel blend of focus for this research was composed of H_2:NH_3:N_2 in a 45:40:15 ratio by volume, which can be obtained from the partial cracking of NH_3 and that has been observed to have similar adiabatic flame temperature and laminar flame speed to conventional methane (CH_4) flames. Spectroscopic studies were used to identify the behavior of the following species of interest due to their importance in developing NH_3 combustion kinematics: OH*, NO*, NH*, and NH_2*. Given that a primary obstacle in the combustion of NH_3 is the production of NO_x and N_2O emissions, focusing on these species can lead to improved overall performance of NH_3-related combustion devices. Recent studies of NH_3-H_2 blend combustion have used tangential swirl burners to observe OH*, NO*, NH_2*, and NH* in simulated internal combustion engine environments. However, the present work used a premixed Bunsen jet burner fitted with a H_2-air pilot flame stabilized on a McKenna burner to study the NH_3 blend combustion under laminar flow conditions. It was found that introducing a low-flow-rate pilot flame stabilized the NH_3 blend sufficiently enough to reach equivalence ratios (ϕ) as lean as 0.58. Around this point the flame became unstable; however,

doubling the pilot flow rate restabilized the NH_3 blend combustion and caused a resurgence in key species production, allowing ϕ to be reduced further to 0.40 before experiencing lean blowout. Variations of OH*, NO*, NH*, and NH_2* spectral profiles as functions of ϕ were generated, and OH* chemiluminescence imaging gave insight into the interactions between the main and pilot flames. It was discovered that the broadband emissions produced as a result of NH_3 introduction into the fuel blend were occurring within the transmission range of the 315-nm bandpass filter used during imaging. Continued refinement of the experimental approach include additional filtration to prevent broadband interference, as well as quantitative diagnostics of such parameters as rate of heat release and laminar flame speed.

ACKNOWLEDGEMENTS

I would like to thank Dr. Waruna Kulatilaka for his assistance throughout not only my research, but also my academic and professional growth. My undergraduate research internships as a member of his group at the Optical Diagnostics and Imaging Laboratory were my first opportunities to participate in graduate-level research. Despite being in the early stages of my academic journey, his guidance allowed me to quickly overcome the learning curves. He has since provided countless resources that have defined my career progression over the years and has helped me overcome the hiccups and setbacks I encountered during my master's studies. I also thank Drs. Lesley Wright and Timothy Jacobs for serving on my thesis committee. Dr. Lesley Wright challenged my interpretation of experimental heat transfer and developed my critical reasoning abilities to the level I needed to complete this research. The graduate classes of Drs. Timothy Jacobs and Eric Petersen prepared me to tackle the complex combustion applications of this work.

Furthermore, I want to thank my colleagues at the Optical Diagnostics and Imaging laboratory whom I have had the chance to befriend and conduct research with these last few years. They are (in alphabetical order by last name): Sidney Davis, Drew Gorman, Ben Gorr, Adi Hardaya, Matt Hay, Matthew Intardonato, Ayush Jain, Gus Kendrick, Gavin Lukasik, Andrew Marsh, Pradeep Parajuli, Christian Schweizer, Manuel Suarez, Will Swain, and Yejun Wang.

Finally, I am grateful for my friends and family for their reassurance throughout my studies. To my fiancé Jonathan Kiker, I want to express my gratitude for his continued encouragement, support, and limitless patience.

CONTRIBUTORS AND FUNDING SOURCES

Contributors

This work was supported by a thesis committee consisting of Dr. Waruna Kulatilaka (chair) and Dr. Lesley Wright of the J. Mike Walker ’66 Department of Mechanical Engineering and Dr. Timothy Jacobs of the Departments of Multidisciplinary Engineering and Mechanical Engineering.

All of the work conducted for the thesis was completed by the student independently.

Funding Sources

Graduate study was supported by the BakerRisk and Avilés-Johnson fellowships from Texas A&M University, as well as the Turbomachinery Research Consortium.

NOMENCLATURE

a.u.	Arbitrary Units
FWHM	Full Width at Half Maximum
HS-IRO	High-Speed Intensified Relay Optics
IR	Infrared
PLIF	Planar Laser-Induced Fluorescence
PIV	Particle Image Velocimetry
SLM	Standard Liters per Minute
ϕ	Equivalence Ratio (volumetric)

TABLE OF CONTENTS

Page

LIST OF FIGURES

Page

LIST OF TABLES

Page

1. INTRODUCTION AND THESIS MOTIVATION

1.1. Environmental Initiatives and the Importance of Ammonia Combustion

Carbon emissions have been linked to atmospheric degradation, agricultural damage, and numerous health concerns [1]. Given these effects, current environmental regulations such as the Paris Climate Accords have aimed at reducing the energy and transportation sector's reliance on carbon-based fuels. Though hydrogen (H_2) boasts high reactivity without the introduction of secondary pollutants, its implementation as an alternative fuel is challenging due to the high costs involved, as well as difficulties in storing and transportation [2]. Ammonia (NH_3) is another alternative that may be more easily employed. With existing facilities for storage and transportation used by the farming industry, NH_3 could be adopted much more readily without significant technological and capital investments [3].

1.2. Ammonia Blends

NH_3 does however still present some difficulties, such as low flame speed and stability, decreased adiabatic flame temperature, and increased formation of nitrogen oxide (NO_x) emissions. To combat these drawbacks, various blends of H_2, NH_3, nitrogen (N_2), and other compounds have been studied [3]. A 45% H_2, 40% NH_3, 15% N_2 by volume blend in particular has shown increased interest. Updated chemical kinetics models have predicted that premixed laminar combustion of this blend performs similarly to methane (CH_4)-air combustion in terms of unstrained laminar flame speed and adiabatic flame temperature for power generation-relevant conditions [4]. Moreover, this blend can be obtained from partial cracking of NH_3, as opposed to the environmentally harmful drilling processes necessary for fossil fuel extraction. Still, the

increased rate of NO_x formation remains an obstacle, and further research into NH_3 combustion remains necessary before application can begin.

1.3. Optical Diagnostics in Combustion Research

Given their non-intrusive nature, optical diagnostic methods have commonly been applied in the study of transient combustion environments. Wiseman et al. studied the previously mentioned $H_2/NH_3/N_2$-air blend combustion alongside conventional CH_4-air combustion [5]. Utilizing OH* chemiluminescence, OH planar laser-induced fluorescence (PLIF), particle image velocimetry (PIV), and updated direct numerical simulations, they were able to provide experimental and numerical validation of the blend and CH_4's near identical unstretched laminar flame speeds, thermal thicknesses, and adiabatic flame temperatures.

Furthermore, the work of Weng et al. focused on the visible range chemiluminescence of laminar NH_3 combustion premixed with O_2 enhanced air and an N_2 co-flow [6]. The visible emissions (400 nm – 700 nm) in the reaction zone were interpreting as largely NH_2*, while the visible emissions above this region in the post-flame zone were dominated by NO_2* during lean combustion and NH_2* during rich combustion.

Fan et al. studied turbulent premixed NH_3-air jet flames stabilized by a stoichiometric CH_4-air pilot [7]. Using CHEMKIN simulations, the three-fold layers of NH_3-air flames were defined: the preheat layer, where the injected NH_3/air is heated and mixed with hot gases from the reaction zone; the fuel-consumption layer, where NH_3 is consumed to form intermediates such as H_2; and the oxidation layer, where intermediates are oxidized to form the final products of combustion (H_2O, N_2, NO). The fuel-consumption layer was defined by overlapping layers of NH_3 and OH coinciding with NH, while the oxidation layer consisted of overlapping layers of H_2 and OH. Given the makeup of these structures, the study used simultaneous NH/OH PLIF, laser

doppler anemometry to experimentally quantify NH_3 flame layer thicknesses as functions of turbulent intensity and Karlovitz numbers. The experimentally acquired turbulent data were then compared to laminar CHEMKIN predictions as functions of turbulent intensity as well.

1.4. Operating Conditions of the Current Work

This research focused on a fundamental approach to NH_3 combustion analysis, quantifying the spectral trends of crucial species used in current chemical kinetics models. Towards this end, neutral testing environments were needed to avoid obscuring the underlying species behaviors. Specifically, premixed laminar combustion in open air at atmospheric pressure and temperature was observed. Furthermore, optical diagnostics forgoing the use of lasers were used to prevent any outside spatiotemporal or spectral influences. Finally, stabilization of the NH_3 combustion was accomplished using a secondary pilot flame.

2. LITERATURE REVIEW

2.1. Recent Studies of Ammonia Combustion

2.1.1. Ammonia Reaction Pathways and Chemical Kinetics

The development and improvement of NH_3 reaction pathways and chemical kinetics have been heavily studied by numerous groups, as these tools currently require refinement to better predict the formation of harmful NO_x emissions. Both experimental and numerical modeling methods have been used to validate proposed pathways and determine dominating NO_x formation/reduction reactions.

One of the earlier works on thermally stimulated NH_3 decomposition pathways was that of Dirtu et al [8]. Using an experimental quartz reactor, 99.98% pure NH_3 was electrically heated to induce breakdown. The products were condensed into a liquid, which was then analyzed using Fourier-transform infrared and Ultraviolet-visible spectroscopy. The spectral footprint of the liquid products was then compared to reported fundamental frequencies of N_2H_4, showing a near identical match. The kinetic mechanisms obtained by the group's previous work detailed this behavior, indicating that an induction period is caused by the formation of the N_2H_4 intermediate, thereby delaying the thermal decomposition of NH_3 into the final N_2 and H_2 products.

Mendiara and Glarborg studied homogenous combustion of premixed CH_4/NH_3-O_2 flames in a preheated gas flow reactor, focusing on reactions between CO_2 and nitrogen-based radicals [9]. N_2 and (for half the experiments) CO_2 were added as bulk flows. Byproducts were assessed using gas analyzers, and experimental results were compared to CHEKIN chemical kinetics models as functions of temperature and equivalence ratio. It was found that NH_3 was converted to NH_2 mainly by reaction (2.1) with the OH radical, with some reformation of NH_3

occurring due to reaction (2.2) with stable hydrocarbon species such as CH_4. The HNO intermediate, formed primarily by reaction (2.3), is stated to be one of the major contributors to NO and N_2 production:

$$NH_3 + OH \rightarrow NH_2 + H_2O \quad (2.1)$$

$$NH_2 + CH_4 \rightarrow NH_3 + CH_3 \quad (2.2)$$

$$NH_2 + O \rightarrow HNO + H \quad (2.3)$$

This work found NO formation through HNO thermal dissociation to be dominant at rich conditions, while HNO reaction with O_2 seeming to dominate the lean regime. Higher flame temperatures saw additional reactions with H, OH, and CH_3 contribute to NO production as well. The following figure visualizes the pathways discussed by [9], where dashed lines represented those pathways only important in experiments involving CO_2:

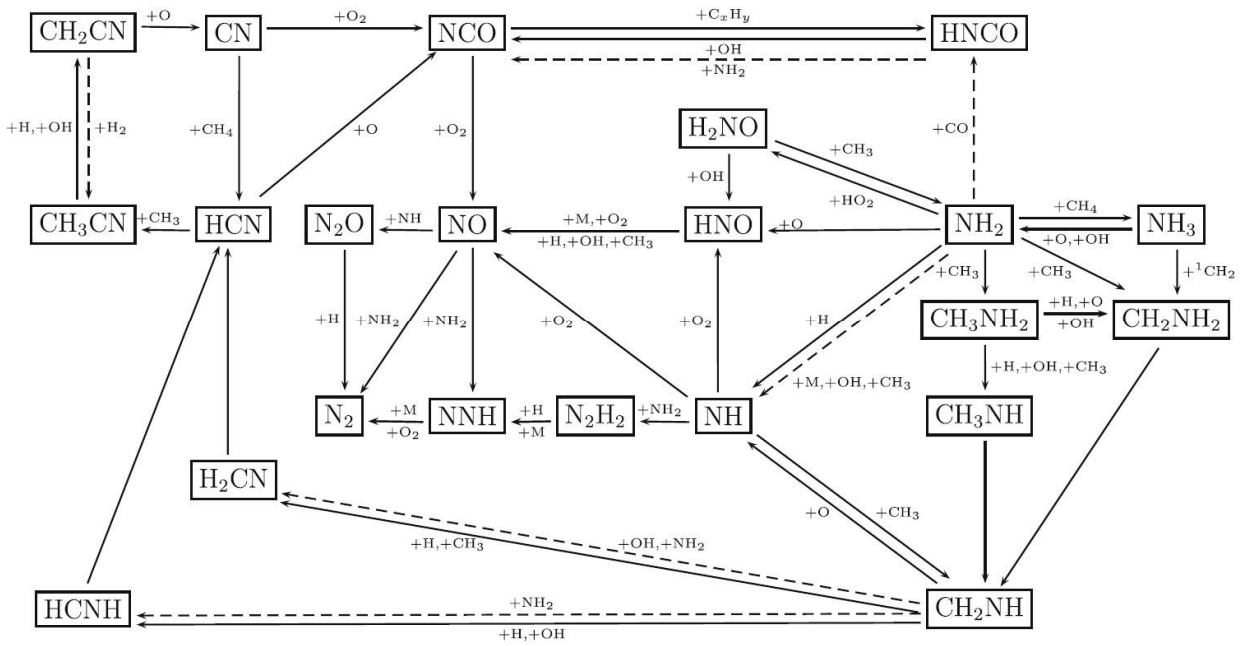

Figure 2.1: Reaction pathways for CH_4/NH_3-O_2 combustion. Reprinted from [9].

The work of Kobayashi et al. summarized advances made in all areas of NH_3 combustion research, including chemical kinetics and the improvement of reaction pathway predictions [10]. In the lean combustion regime, the breakdown of NH_3 to NH_2 by H atom abstraction has been found to occur primarily through reaction with the OH radical, validating the results of [9]. Secondary consumption then occurs through reaction with atomic H and O, with the concentration of these two radicals affecting the final products formed: the surplus of O/H during lean combustion has been speculated to inhibit NO reduction by NH_i (i = 0, 1, 2) reactions, instead leading to NO formation through the HNO intermediate as stated by [9]. HNO in turn was found to be formed largely by the reaction of NH_2 with atomic O, going on to produce NO through thermal dissociation or reaction with H, OH, or O_2. These reaction pathways involving HNO were stated by Kobayashi to be the "dominant NO production path in NH_3/air flames under all conditions." During rich combustion, it was suggested that the relative lack of O atom yielded

increased production of H_2 due to H abstraction from NH_3, eventually producing a surplus of N atoms. This caused the Zeldovich mechanism (reactions (2.4) and (2.5)) and extended Zeldovich Mechanism (reactions (2.4), (2.5), and (2.6)) to become dominant:

$$N_2 + O \Leftrightarrow NO + N \tag{2.4}$$

$$O_2 + N \Leftrightarrow NO + O \tag{2.5}$$

$$N + OH \Leftrightarrow NO + H \tag{2.6}$$

This famous pathway of NO_x formation requires sufficient nitrogen concentration and is highly temperature dependent, typically contributing minimally to NO production for conditions under 1800 K – 2000 K. Reaction (2.4) is considered the rate-determining reaction of the Zeldovich Mechanism, while reaction (2.5) occurs more slowly and is dependent on sufficient O_2 supply [10]. The addition of reaction (2.6) in the extended Zeldovich mechanism meanwhile only minimally improves NO formation predictions since this reaction represents a modest portion of the total OH interactions, which have been stated to be primarily concerned with NH_3 breakdown.

To quantify the effects of NH_3 dilution in an NH_3/H_2 fuel blend, Mashruk et al. used a tangential swirl burner to observe the concentrations of important species (NO, NO_2, NH_3, and N_2O) at atmospheric pressure and 288 K [11]. During rich combustion, it was found that reduced O/H presence and lower temperatures decreased the production of NO. The dominance of the Zeldovich mechanism in the rich regime provides some clarification of this observed trend: the decrease in sufficient O/H radicals for reaction with N or N_2, as well as the associated lower flame temperatures of excessively rich combustion, rob the Zeldovich mechanism of its primary

NO formation catalysts. The study also found that those mixtures higher in NH_3 content exhibited slower burning velocities as a result of the lowered flame temperatures and decreased radical species, generating fewer chain branching reactions (these being largely responsible for increased flame propagation rates).

Alnasif et al. studied the chemical kinetics of an 85% NH_3 and 15% H_2 by volume mixture with air in a premixed swirl burner at standard atmospheric conditions [12]. Excited species with considerable impact on the formation of NO_x emissions were focused on, namely NO*, OH*, NH*, and NH_2*. The experimental data was compared to the numerical results of seven recently published kinetic mechanisms:

Table 2.1: Parameter-wise chemical kinetics model optimization. Reprinted from [12].

No	Kinetic Model	No. of Reaction	No. of Species	Fuel Mixture	Optimization Parameter	Parameter's Effect
1	A. Bertolino et al.	264	38	NH_3	LBVs, Ignition delay time, speciation measurements	Optimization of N_2 chemistry based on pressure-dependent reactions
2	B. Mei et al.	264	38	$NH_3/NO/N_2$	LBVs, Markstein length, NO_x formation	Equivalence ratios
3	X. Han et al.	298	36	NH_3, NH_3/N_2O	LBVs, Speciation measurements, NO_x formation	Equivalence ratios, N_2O mixing ratios
4	X. Zhang et al.	264	38	NH_3, NH_3/H_2	NO_x formation	Lean and rich conditions, H_2-enriched in fuel
5	A. Stagni et al.	203	31	NH_3	LBVs, ignition delay time, speciation measurements	Optimization of NH_3 oxidation mechanism in full range of operating conditions
6	X. Han et al. (2019)	130	20	NH_3 + syngas	LBVs, ignition delay time, NO_x measurements	Equivalence ratios
7	S. de Persis et al.	647	103	CH_4	LBVs, NO_x measurements	Equivalence ratios, elevated pressure

The study concluded that the integrated intensities of the excited species studied, as well as the concentrations of NO and N_2O, increased with Reynold's number. Reaction (2.7) and reaction

(2.8) were found to be the primary causes of NO and N_2O formation respectively, with N_2O being produced by NO combination given sufficient NH radical density:

$$HNO + O_2 \rightleftharpoons NO + HO_2 \quad (2.7)$$

$$NO + NO \rightleftharpoons N_2O + H \quad (2.8)$$

These findings further validate the HNO predominance in NO formation pathways discussed by [9] and [10].

2.1.2. Ammonia Blends as Potential Carbon-Based Fuel Alternatives

The overview completed by Kobayashi additionally summarizes recent studies on combustion performance improvement using both carbon-free and conventional hydrocarbon-based NH_3 blends, these blends representing an important segway in the gradual phasing out of carbon fuel reliance [10]. For blends of NH_3 and H_2 in spark ignition engine and combustor studies, performance was optimized for blends with increased H_2 content. This yielded exponential improvements in laminar burning velocity compared to pure NH_3 combustion due to the previously mentioned chain branching behavior [11]. For fundamental studies of mixtures involving carbon, NH_3 doping produced lowered CO_2 emissions compared to pure hydrocarbon combustion, although the consequence of even small amounts of NH_3 addition was exceedingly high concentrations of NO in the exhaust. Furthermore, although the addition of the hydrocarbons improved the flame speeds and temperatures of the reaction compared to pure NH_3 combustion, greater NH_3 content predictably limited these improvements. Application studies in engines yielded improved performance of NH_3/CH_4 blends premixed with air, although flame stability and ignition became problematic with higher NH_3 concentrations. A proposed solution

to this problem was oxygen supplementation, which yielded improved laminar burning velocities, flame temperatures, heat flux rates.

Lhuillier et al. studied premixed combustion of NH_3/H_2 blends utilizing a four-cylinder four-stroke SI engine (though only fueling and operating a single cylinder during this study) and used a Fourier-transform infrared spectrometer to measure NO_x and NH_3 emissions [13]. Stable operation (coefficient of variance of the engine's net indicated mean effective pressure equal to or less than 5%) could be achieved for stoichiometric NH_3/air at slightly supercharged conditions, and most tested conditions showed a coefficient equal to or below 3%. Excessively lean conditions however required increased H_2 percentage, and greater advanced spark timing was required for mixtures high in NH_3 due to the decreased laminar burning velocities. The optimum power output was observed for supercharged operation and for fuel blends of 20% H_2 or less, with higher H_2 percentages leading to greater rates of heat loss. The emissions of NH_3 were minimal for lean combustion near stoichiometry, with increased H_2 percentage shifting this minimal point farther to the lean side but increased dramatically once reaching rich or excessively lean conditions due to dwindling combustion efficiency. NO_x emissions meanwhile were diminished for rich combustion conditions with greater NH_3 percentages, likely due to the diluting effects of excessive fuel and NH_3 on the flame temperatures, consequently preventing the thermal NO_x pathway. The maximum NO_x condition was found to be just shy of stoichiometry.

Kurata et al., one of the first to study pure NH_3-air combustion and exhaust gas analysis in gas turbine applications, compared the performance differences between NH_3-air and NH_3/CH_4-air combustion [14]. The single shaft, 50 kW-class micro gas turbine used was utilized a heat regeneration cycle and was rated for 80,000 rpm rotational speed. Before startup, the

turbine lubrication oil and vaporizer water were heated up to prevent increased hot loss to the surroundings. Due to the instability and limited combustible range of NH_3, kerosene firing was used to start up the engine. After power generation was stabilized, NH_3 was injected at increasing amounts until the entirety of the kerosene supply had been displaced (while maintaining stability). The power produced by NH_3-air combustion could then be gradually increased. This start up procedure is depicted below:

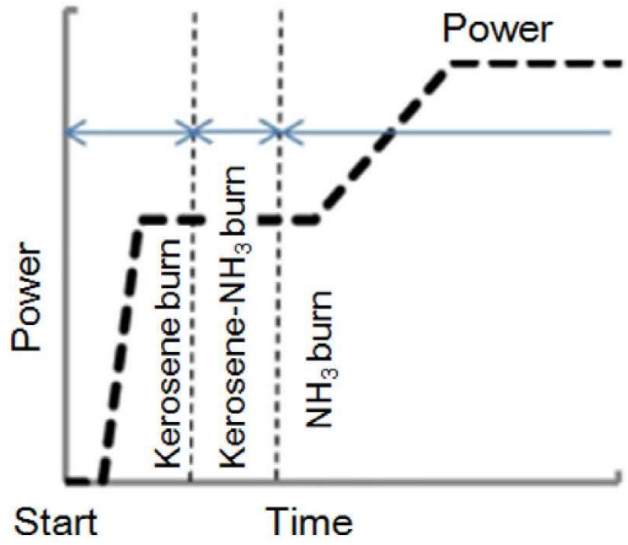

Figure 2.2 Example NH_3-air gas turbine start up procedure. Reprinted from [14].

After exiting the turbine, the exhaust gases underwent selective catalytic reduction before analysis. The engine was operated for NH_3-air combustion for ranges of 18.4 kW – 44.4 kW and 70,000 rpm – 80,000 rpm, with NO at the turbine outlet increasing with increasing electric power or decreasing rotation speed. The NO_x emissions (for a rotating speed of 78,000 rpm), after selective catalytic reduction, dropped down from 1100 ppm to 10ppm. For a mixture of NH_3/CH_4 with the engine operating at 75,000 rpm and producing 31.4 kW, a trend was made of NO

emissions as a function of NH_3 fuel ratio, which was defined as the ratio of the lower heating value of the NH_3 in the fuel to that of the whole fuel blend. The NO emissions increased with this ratio until reaching a peak of about 100 ppm for a fuel ratio of 0.65. The HCN emissions were about 20 ppm, but would decrease as operating power increased, eventually reaching negligible levels. With the engine operating at 80,000 rpm, the NH_3-CH_4 mixture was able to generate between 15.8 kW and 41.8 kW, compared to a roughly 30.0 kW to 40.0 kW range for NH_3-air. The NH_3/CH_4-air blend also saw an increase in thermal and combustion efficiency at 80,000 rpm for all power levels tested.

2.1.3. Relevant Computational and Modeling Studies

Aiming to overcome the limited operating conditions pure NH_3 internal combustion engine studies, Lee and Song utilized the following strategy: divide the NH_3 combustion process into four theoretical steps, develop a model to validate the proposed concept's viability, study the effects of injection timing and fuel quantity, and predict the production of NO as a function of these injection timings and fuel quantities for each of the four combustion steps [15]. The proposed combustion steps are depicted in the figure below:

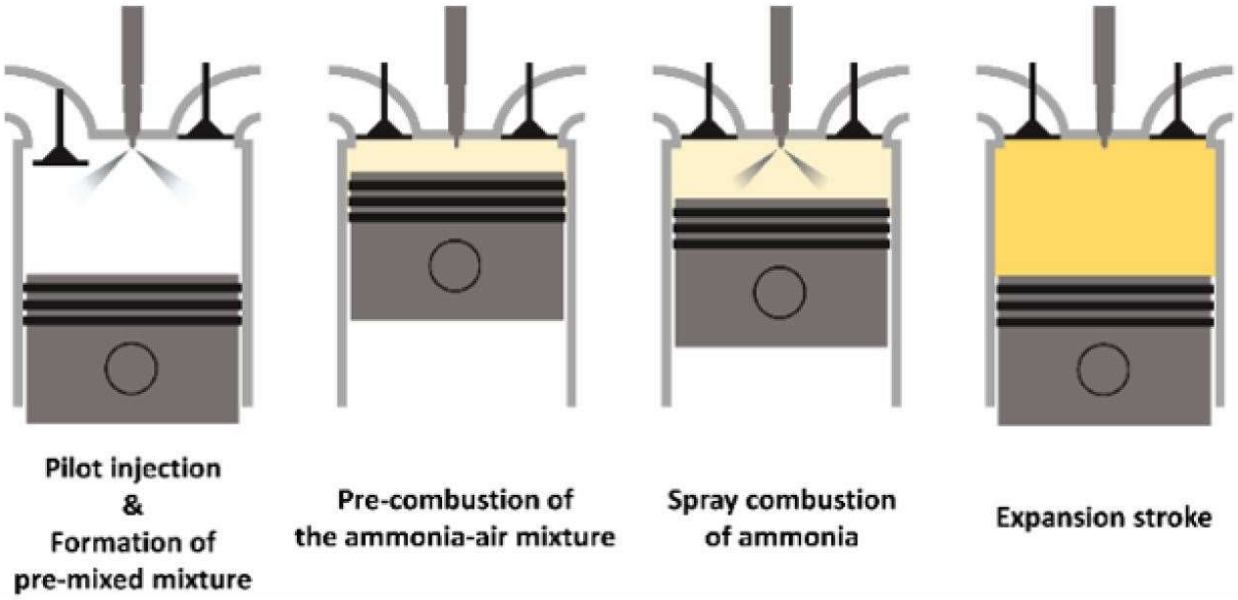

Figure 2.3 Potential four-phase (left to right) NH_3 combustion strategy. Reprinted from [15].

During the intake stroke in phase one, traces of NH_3 would be injected to homogenize with the air (referred to Lee and Song as "pilot injection"). The compression stroke in phase two then raised the cylinder pressure and temperature, ideally causing kinetically driven auto-ignition of the mixture (referred to as "pre-combustion") due to the high vapor pressure of NH_3. With these conditions sufficient to burn greater quantities of NH_3, the remaining NH_3 stream would be injected shortly either before or after the start of pre-combustion. When the piston reached its maximum height at the end of pre-combustion, this position was referred to as "top dead center" and was described in terms of crank angle degrees before or after reaching the apex at 0°. In the fourth and final phase, the O_2 left unburnt after pre-combustion was consumed by the main NH_3 stream. The periods of NO formation for each of the four phases were as follows: pre-combustion, where NO was formed by the auto-ignition of trace NH_3 pilot injection; reduction, during initial spray formation when NO in the ambient regions of the modeled cylinders would

be reduced by the main spray excess NH_3; combustion, when NO was formed through combustion reaction of NH_3 with air; and thermal, when NO would be formed through the reaction of excess N_2 in the air following combustion, which was highly dependent on the temperatures (and therefore equivalence ratios) reached during the combustion phase.

The viability of the proposed combustion strategy was confirmed through a quasi-dimensional spray modeling, as well as models of the chemical reactions and thermodynamic environment in the cylinder, while assuming a uniform pressure profile in the cylinder. The spray model was defined from intake valve closure to exhaust valve opening, with consistent thermodynamic properties, gaseous homogenous reactions, and well mixed pilot NH_3/intake air. It utilized sub-division zones of axial and radial spray propagation and assumed constant spray velocity until the start of break up, at which the flow began to evaporate. The chemical reaction model used was a version of that developed by Mathieu et al. [16] with modified coefficients from Klippenstein et al. [17] and Miller and Bowman [18] to improve the thermal deNO_x approximation. It considered both NO production through fuel-bound and thermal methods, as well as NO reduction through reaction with NH_3 in low temperature regions. The thermodynamic environment of each sub-divided ambient and multiple-fuel zone was determined by solving a series of ordinary differential equations relating to changing cylinder pressure, volume, and heat transfer rates simultaneously. The study found that increased pilot injection of NH_3 yielded an increase of the simulated engine's gross indicated mean effective pressure as well, this being a measure of the engine's capacity to do work irrespective of cylinder displacement size. The feasible range of injection timing also increased. Given a fixed pilot injection rate, an increase in the main injection of NH_3 resulted in greater difficulty initiating pre-combustion for earlier injection timings. With regards to NO formation, the timing of injection yielded a greater effect

on total NO production than varying engine loading. The combustion NO phase was generally the greatest contributor to NO formation, except for injection timings between 10° and 0° before top dead center when thermal formation of NO tended to dominate.

From a more fundamental approach, the effects of pilot and main flame interaction have been studied numerically, with the findings compared and validated by previously obtained experimental data [19]. The experimental setup, which the numerical model was based on, used a CH_4-air central jet burner with a 1.5-mm diameter accompanied by a CH_4-air pilot with a 61-mm diameter. The main flame equivalence ratio was tested at 0.4, 0.7, and 1.0, while the pilot equivalence ratio was maintained at near stoichiometric (0.9) except for one case where it was lowered to 0.7. The flames were tested and modeled under atmospheric conditions, with the unburnt gas temperature at 300 K. Two laminar single-dimensional ANSYS CHEMKIN models were used to predict the interactions of the pilot and main flames: a freely propagating flame simulation provided feedback on the effects of mixing hot products between the pilot and main flames, while a counterflow simulation characterized the effects of back-support (additional heat, non-oxidized fuels, and radical species supplied by the pilot flame) and flame stretch. Additionally, the DRM22 chemical kinetic mechanism was used for all calculations. Since the pilot's adiabatic flame temperatures were comparable when burning at equivalence ratios of 0.7 and 0.9, it was possible to distinguish between those effects on the main flame due to the pilot's chemical composition and those due to the pilot's hot gas temperatures.

Firstly, in terms of chemical composition, the results indicated that the pilot flame can aid in main flame stability through zone mixing behavior. Separate from the reaction zone of the main flame, the reaction zone of the pilot flame encompassed the regions of hot pilot coflow and the outer mixing region of the main flame. The local equivalence ratio of this pilot reaction zone

was found to be nearly directly proportional to the pilot mixing ratio, this ratio being a non-dimensionalized term to quantify the level of pilot/main flame mixing in the pilot reaction zone. When the pilot equivalence ratio grew significantly greater than that of the main flame, the increase in the mixing ratio between the two flames helped sustain the main flame at conditions previously below the flammability limit.

Meanwhile, the pilot hot gas composition only minimally effected the main flame burning velocity; though decreasing the pilot equivalence ratio lowered the mass fractions of supplemental radical species and non-oxidized H_2, the overall flame speed remained the same. The composition-dependent reaction and diffusion rates of the mixed pilot reaction zone were actually found to be lower than that of the pure main flame. Instead, numerical simulations indicated that locally decreased mixture density in the pilot reaction zone caused by the hot gases supplied was responsible for increasing the main flame's burning velocity. In addition to this thermal benefit, the pilot was also found to prevent entrainment of cold ambient air in the main flame reaction zone.

Finally, the effect of increasing main flame strain rate were quantified. Higher strain rates served to increase the rates of heat transfer and reactive radical mass transfer between the pilot and main flames. The direction, positive or negative, of this interaction was determined by the temperature relationship between the main and pilot flames, which likewise was based on the equivalence ratio of the main flame (since the pilot flame equivalence ratio remained unchanged). For ultra-lean main flames at equivalence ratios previously below the flammability limit, the hot gases supplied by the pilot were at a higher temperature than the main flame. This led the direction of heat transfer (and radical mass transfer) to progress from the pilot flame to the main flame. The increased rates of transfer produced by greater strain rates thus served to

improve the main flame's reactivity and burning velocity. Main flame equivalence ratios just below stoichiometric yielded temperatures similar to the pilot flame, which minimized the rate of heat or mass transfer in either direction. For rich flames meanwhile, the main flame temperature was greater than that of the pilot flame, causing the direction of heat and radical mass transfer to progress from the main flame to the pilot flame (i.e., a loss for the main flame). Therefore, as strain rate was increased, the main flame burning velocity and reactivity decreased under these conditions.

One primary source of loss and uncertainty in piloted flame experiments is that caused by heat transfer between the pilot flame and the burner, since generally the pilot flame covers a significant surface area of the room-temperature burner. Brackmann et al. hoped to mitigate these losses through N_2 dilution of the pilot steam, lifting the pilot flame off the burner surface [20]. This could however alter the chemistry or spectral characteristics of the pilot flame.

2.2. Recent Studies of Optical Diagnostics in Ammonia Combustion

Primary advantages of optical diagnostic methods include their in-situ measurement applications, potential for spatiotemporal resolution, and minimal disturbance of transient flow fields. Varying forms of optical techniques have been applied to the analysis of NH_3 combustion, including PIV [5], schlieren imaging [21], and numerous spectroscopic techniques [8], [11]. These studies have provided valuable insight into the combustion behavior of NH_3 blends, including characterizing the injection velocities and equivalence ratios of the lean blowout limit as functions of equivalence ratio and NH_3 fuel fraction, respectively (figure 2.4 and figure 2.5).

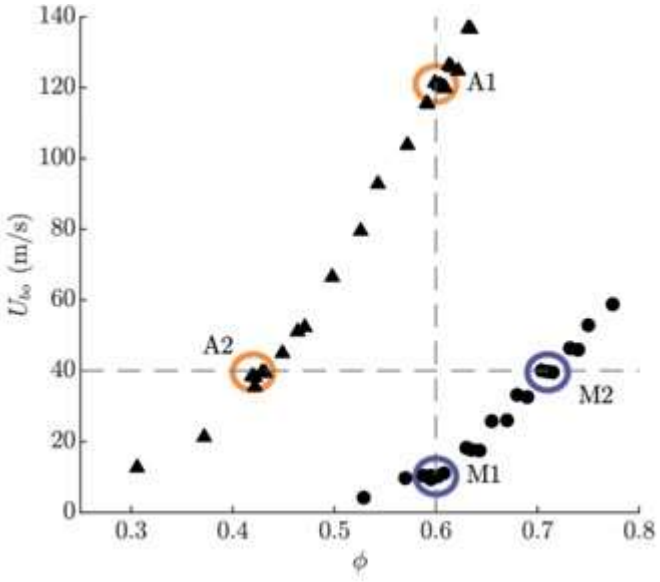

Figure 2.4 Blow-out curves for 45% H_2, 40% NH_3, 15% N_2 blend (triangles) and CH_4 (circles) as functions of equivalence ratio. Reprinted from [5].

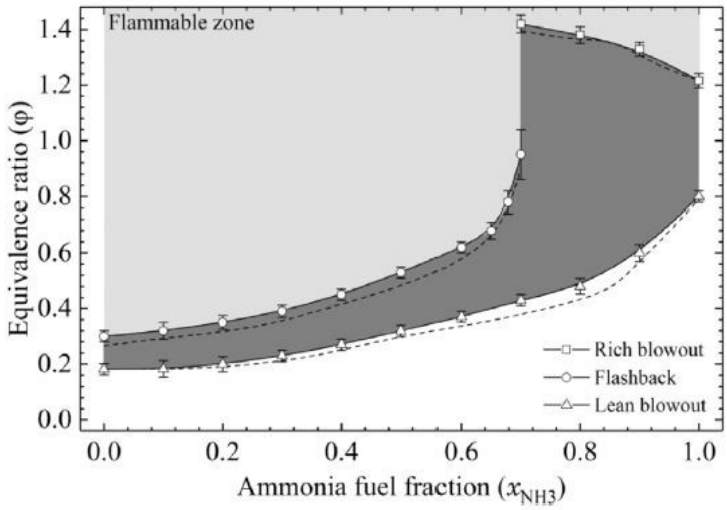

Figure 2.5 Blow-out curves for various $H_2/NH_3/N_2$ fuel blends as a function of NH_3 fuel fraction. A 0.4 NH_3 fuel fraction corresponds to the previously addressed 45% H_2, 40% NH_3, 15% N_2 blend. Reprinted from [22].

Spectroscopic methods in particular have been valuable given their ability to characterize the progression of key species involved in NO_x formation pathways. The experimental data

provided by these optical approaches can be used in the validation and improvement of such chemical kinetic and combustion models as were discussed earlier.

OH*, NO*, NH_2*, and NH* chemiluminescence have been used in conjunction with numerical kinetics models [8], with their roles in the breakdown of NH_3 and formation of NO_x having been described earlier. The work of Zhu et al. provided chemiluminescence analysis over a greater range of experimental conditions than had been reported for NH_3/CH_4 combustion at the time [23]. Zhu et al. used the same OH (A-X) emissions as commonly used in studies of hydrocarbon combustion, with small congregated (1,0), (2,1), and (3,2) bands visible in the 275 nm – 300 nm range, as well as a significant peak from the (0,0) and (1,1) bands around 310 nm. However, once nitrogen was introduced as with NH_3-based combustion, the (1,0), (2,1), and (3,2) bands become obscured by overlapping vibrational NO A-X (3,0), (4,0), (5,0), and (6,0) emissions. The remaining NO (0,0), (1,0), and (2,0) emissions between 200 nm and 250 nm seemed to remain distinct from any significant emission lines. Zhu et al. noted that, given the distance between their experimental set up's point of optical access and the flame reaction zone, some of the chemiluminescence signature of the weak NO absorption band in the 220 nm – 225 nm range could be absorbed by reactant NH_3. Several NO A-X bands were used to mitigate this issue. An additional effect of NH_3 combustion was the development of a distinct NH (0,0) band at 336 nm. As the concentration of NH_3 was increased, the emissions of carbon-based radicals predictably vanished. Moreover, a significant broadband signal appeared over the entire visible wavelength range, continued into the infrared (IR), and were responsible for the yellow/orange color observed in the high NH_3 content flames (figure 2.6).

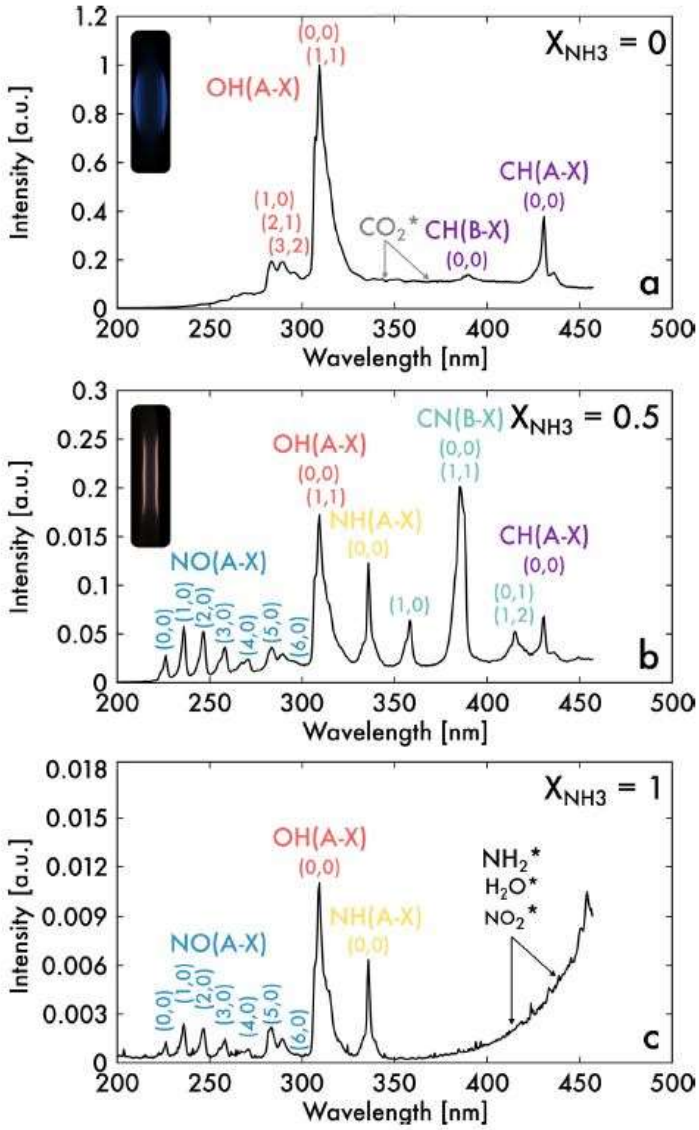

Figure 2.6: Chemiluminescence spectra for pure CH_4 (top), half CH_4/NH_3 (middle), and pure NH_3 (bottom). Reprinted from [23].

Characterization of the species emissions occurring in the visible and IR range included the works of Hayakawa et al. [24] and Paulsen et al. [25]. Hayakawa et al. compared experimental and numerical data, using a 14 mm diameter nozzle-type burner with surrounding 55 mm x 140 mm quartz tube, as well as an extremely rich H_2-air pilot to stabilize premixed NH_3-air combustion. Notable spectral peaks were detected at 543 nm, 571 nm, 604 nm, 630 nm,

and 665 nm, these being previously linked to those emissions of the NH_2 α band [26]; no mention was made of spectrometer intensity calibration. Emission lines associated with that of H_2O vapor were also observed to occur in the IR range at roughly 735 nm, 825 nm, 900 nm, and 920 nm [27]. Hayakawa et al. overlayed the spectrum of NH_3 and that of H_2O vapor to demonstrate the points of similarity, with the peaks of the NH_2 α band emissions indicated:

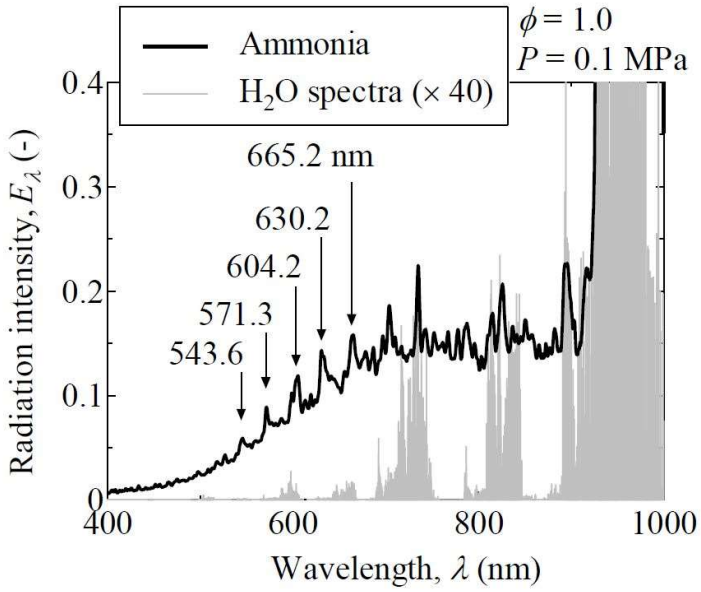

Figure 2.7: NH_3 spectrum with H_2O spectrum overlayed and NH_2 α bands indicated. Reprinted from [24].

In addition to NH_2* and H_2O*, NO_2* emissions have also been theorized to play a part in the broadband emission [23]. The fundamental work from Paulsen et al. recognized a gradual increase in NO_2 recombination emissions after 400 nm, reaching a maximum around 650 nm, with thermal emissions from NO_2 at 1289 K exponentially growing after about 600 nm and theorized to continue increasing until at least 950 nm [25]; their photomultiplier-spectrometer

assembly was calibrated with respect to an Eppley Lab 1000-W quartz iodine lamp. Figure 2.8 depicts the broadband emissions produced by the NO_2 recombination and thermal emissions:

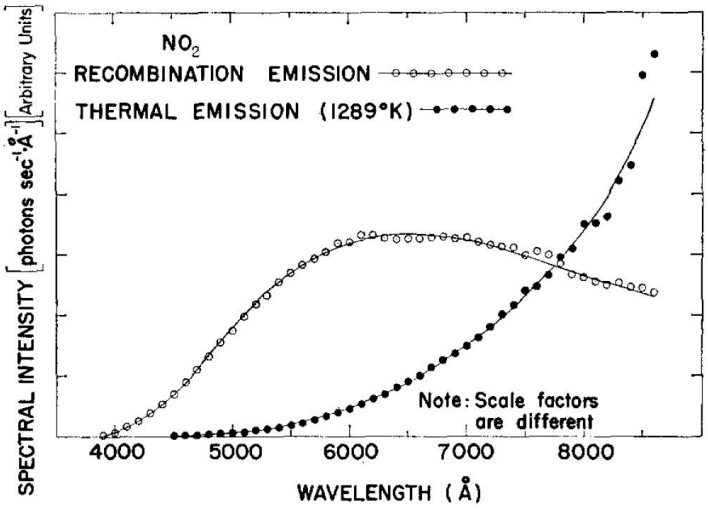

Figure 2.8 Spectrum of NO_2 recombination and thermal emissions. Reprinted from [25].

In general however, the emission contributions of H_2O and NO_2* have generally been assumed to be negligible compared to that of NH_2*, with some studies interpreting the entire visible spectrum as pure NH_2* emissions [6]. Other studies such as the work by Pugh et al. have used bandpass filters to isolate one of the NH_2 α bands [28]. Pugh et al. approximated the behavior of primary flames in staged combustors using a swirl burner with varied inlet pressure and temperature conditions. To characterize NH_2, the 630 nm α band was captured using a 632 nm filter with a $\pm$ 10 nm bandwidth, citing [24] to conclude that the interference of H_2O in this region would be negligible. OH* and NH* measurements were made using 315 nm $\pm$ 15 nm and 337 nm $\pm$ 10 nm filters, respectively. Additionally, for any ranges of overlap for the filters, the transmittance was confirmed to be equal to or less than 1%.

3. EXPERIMENTAL METHODS

3.1. Burner Details

The primary components used during this research were a Holthuis and Associates flat flame burner (hereafter referred to as the McKenna Burner), a Nikon DSLR camera, a Teledyne Princeton Instruments IsoPlane 320/PI MAX 4 ICCD spectroscopy system, and an OH* chemiluminescence imaging system composed of a Photron Fastcam SA-Z camera, LaVision High-Speed Intensified Relay Optics (HS-IRO), and OH bandpass filter.

The McKenna burner allows for premixed or diffusion combustion through a porous sintered metal plug, with this work utilizing its premixed combustion capabilities. A thin pipe way in an Archimedean spiral served to cool the burner to minimize temperature gradients and prevent overheating, with this study utilizing water as the coolant. As a custom alteration, a central jet burner was added to introduce the premixed fuel blend, while the sintered plug was used to introduce a secondary H_2-air pilot flame. The images in the figure below depict a simplistic cut out of the base burner, as well as a picture of the custom burner used during this work.

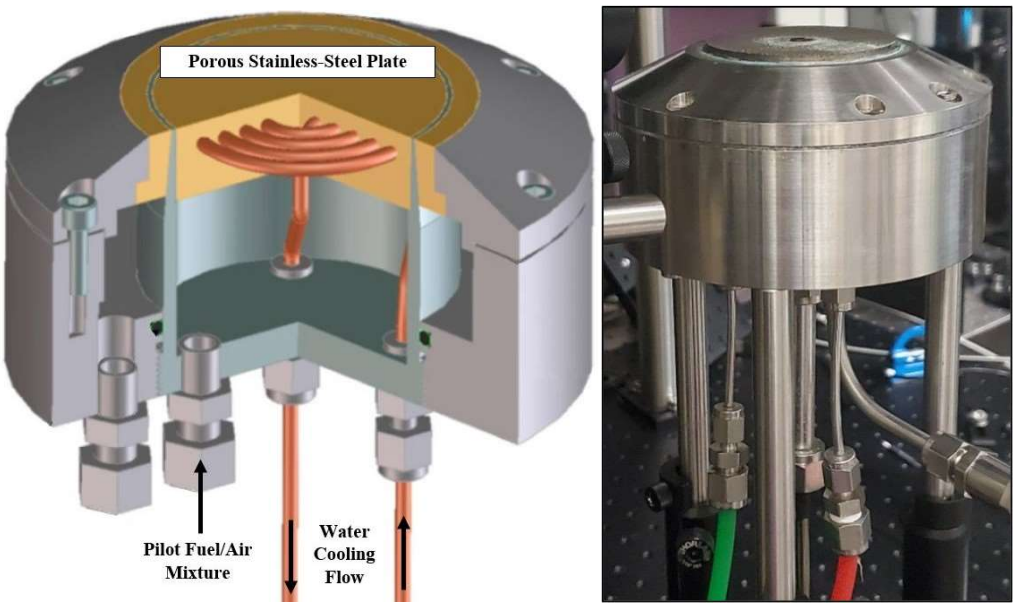

Figure 3.1 Base McKenna burner diagram with cut out to view internal flow pathways (Left) and custom-made piloted-flame burner used for this research (Right). Base McKenna burner diagram adapted from [29].

While other studies have used H_2-air piloting to stabilize NH_3 combustion under a range of operating pressures [24], this work is unique in its observation of H_2-air piloted $H_2/NH_3/N_2$ blend combustion under non-extreme, atmospheric, and laminar conditions to spectrally determine the fundamental flame behavior.

MKS GE-50 elastomer sealed digital mass flow controllers were used to adjust the species volumetric flow rates of both the $H_2/NH_3/N_2$-air main flame and the H_2-air pilot flame, where the flow rates were specified in terms of standard liters per minute (SLM). Both the $H_2/NH_3/N_2$ blend and air were injected through the central jet to yield a premixed laminar flame at atmospheric pressure. For the pilot flame, both H_2 and air were injected through the secondary pilot pathway, where the porous stainless-steel plate allowed the resultant H_2-air flame to envelope the entire flat surface surrounding the central jet. Here ϕ was defined as the volumetric fuel-to-oxidizer equivalence ratio of the main flame, with the $H_2/NH_3/N_2$ blend as the fuel and air

as the oxidizer. Equation (3.1) details the stoichiometric equation that was balanced to determine the necessary ratio of total supplied fuel and air, M_{fuel} and M_{air} respectively, to obtain the desired ϕ. To achieve these ϕ, the central air flow rate (29% O_2 and 71% N_2 by volume) was altered while the fuel flow rate M_{fuel} was kept constant at 3.24 SLM (comprised of 45% NH_3, 40% H_2, and 15% N_2 by volume). The stoichiometric ratio of fuel blend to air was determined to be 1.000:2.499 from the atom balance. Using these constant values, the total air flow rate M_{air} could be increased or decreased to adjust ϕ using equation (3.2).

$$a\left(H_2 + \frac{40}{45}NH_3 + \frac{15}{45}N_2\right) + b(O_2 + 3.76N_2) \rightarrow cH_2O + dN_2 \quad (3.1)$$

From atom balance: $a = (6/7)b$

$$M_{fuel} = a\left(1 + \tfrac{40}{45} + \tfrac{15}{45}\right) = \left(\tfrac{6}{7}b\right)\left(1 + \tfrac{40}{45} + \tfrac{15}{45}\right)$$

$$M_{air} = b(1 + 3.76)$$

$$\phi = (M_{fuel}/M_{air})/(1.000/2.499) \quad (3.2)$$

The porous plug was then used to introduce a secondary H_2-air pilot flame at atmospheric conditions. This pilot flame was kept at stoichiometry, with two distinct pilots being utilized during the course of this work: a "low-flow-rate pilot" with H_2 and air flow rates of H_2-2.0 SLM and air-4.76 SLM respectively, and a "high-flow-rate pilot" with H_2 and air flow rates of H_2-4.0 SLM and air-9.52 SLM respectively. The specific flow rates used, as well as a simplistic diagram of the overall setup, are shown in figure 3.2.

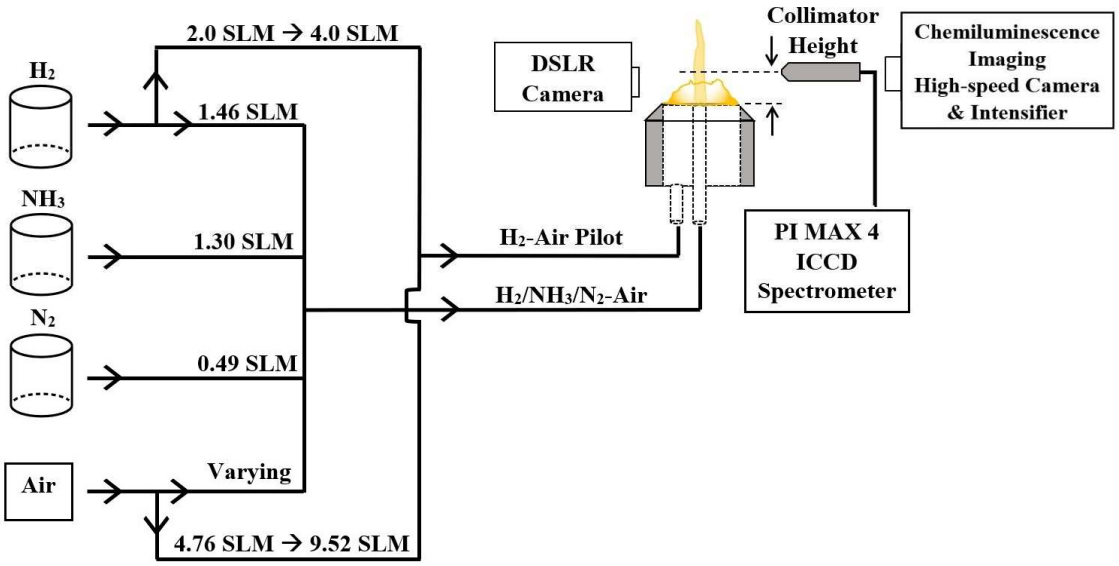

Figure 3.2 Simplistic experimental setup and gas flow pathways diagram.

3.2. Qualitative Visual Characterization

Qualitative visual characterization was completed using the Nikon DSLR camera with the exposure manually controlled. The shutter was set to its longest exposure time of 0.2 seconds to maximize light intake given the extremely faint combustion events, especially during increasingly lean ϕ. Similarly, the f-number was minimized at f/1.4, which allowed the largest possible aperture diameter. This method not only further optimized light collection but also ensured a small depth of field to focus only on the flame and not any background material. Finally, ISO 100 setting was used to minimize noise.

3.3. Emission Spectroscopy

Emission spectroscopy was performed using the Teledyne Princeton Instruments IsoPlane320/PI MAX 4 ICCD spectroscopy system. A fiber optic cable with an attached

collimator was used to direct the collected emission from the combustion event onto the spectrometer. Spectral wavelengths were automatically calibrated using the built-in IntelliCal software and a mercury lamp. Though automatic calibration for quantum sensitivity was only available for visible wavelength emissions, since the species of interest for this work included those with spectral signatures in the ultraviolet region, quantum sensitivity correction was performed during data analysis. The gate width was maintained at 1 ms, and the entrance slit was at 50 μm. On-CCD averages of 100 exposures per frame were used to obtain an averaged spectrum representing the general emission behavior of the flame. Additionally, the ICCD gain was set at 100% given the low-light conditions of the combustion events studied, particularly at extremely lean conditions. These settings yielded spectra of intensity counts in terms of arbitrary units (a.u.) as functions of wavelength (nm). Four key species were analyzed during this work, specifically NO*, OH*, NH*, and NH_2*. The 312-nm OH* band and 337-nm NH* band were used. As was addressed by the work of [23], the 250 – 300-nm range may contain residual OH* emissions; therefore, the NO* emissions produced only along the 200 – 250-nm range were used to avoid this potential overlapping OH* (the OH* band chosen likewise avoids this region of NO* interference). As for NH_2*, this work utilized the 630 nm α band emission previously reported in literature [24], [28]. It should be noted that the spectral analysis only applies to the excited states of each species since the emissions observed are produced when the excited species release their excess energy via chemiluminescence emission when returning to ground states.

During data reduction, the background spectra (which were collected by obstructing the spectrometer's field of view) were subtracted from the collected flame spectra. Afterward, the background-removed spectra were intensity calibrated to compensate for the combined effects of PI-Max 4 and grating quantum sensitivities. A system efficiency curve was developed (figure 3.3), with the emission data at each point normalized by the respective efficiency to obtain corrected spectra for each ϕ. Figure 3.4 demonstrates the effects of system efficiency correction as a function of wavelength on the spectrum obtained at $\phi = 1.35$, as well as a spectrum obtained with the same air and fuel constituent flow rates but with the NH_3 supply cut off. The NH_3-free spectrum was collected using on-CCD averages of 50 exposures per frame and with ICCD gain at 50%. The inclusion of NH_3 in the fuel blend produced a noticeable broadband feature between 400 – 900 nm, in comparison to the NH_3-free spectrum which lacks this feature. It should be noted that the drastic increase in emission intensity observed after ~900 nm were artificially inflated as a result of the intensity calibration performed. At this point, the system total efficiency dwindled to fractions of a percent, resulting in essentially dividing the spectral intensities by zero. For this reason, the remaining spectra figures and any spectral analyses were cut off at 900 nm to prevent inaccurate exaggeration.

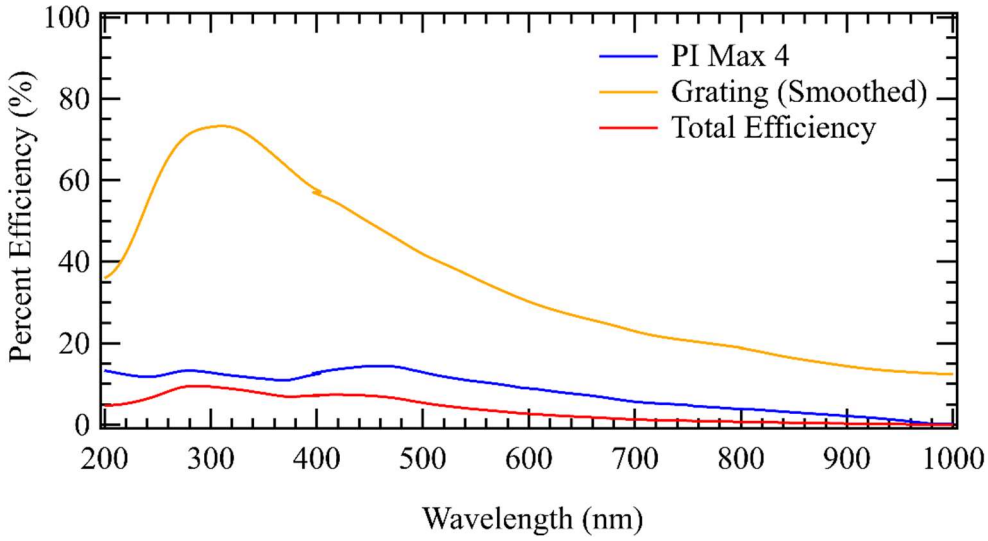

Figure 3.3 Spectrometer setup's Pi Max 4 camera, smoothed grating, and total efficiency curves as functions of wavelength.

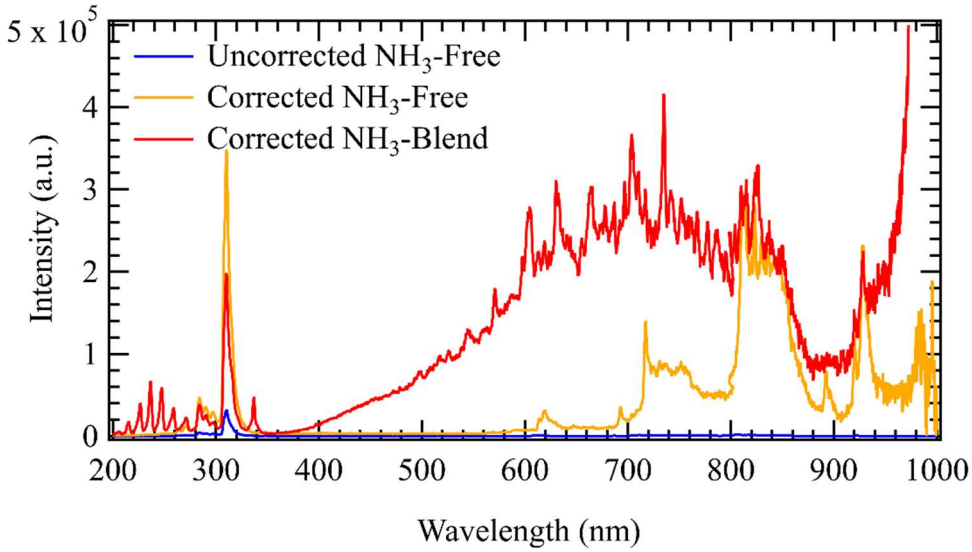

Figure 3.4 Example spectrum before and after intensity correction for quantum efficiency. Collected at $\phi = 1.35$ for the no pilot case. NH_3-free flames utilized the same fuel and air flow rates but with the NH_3 supply cut off.

The corrected, background-removed emission data were then spectrally integrated across the full width at half maximum (FWHM) wavelength ranges of each of the key excited species' emissions,

except for NO which was integrated along its entire discussed emission range (200 – 250 nm). This process reduced a spectrum collected at a particular ϕ to a single intensity data point for each of the key species. This method of integrated intensity analysis, rather than relying on the peak intensities of each emission band, was more reliable for comparison than fluctuating peak intensities. Other works have used similar methods for spectral diagnostics [23]. A plot could then be formed of background-removed integrated species intensities as functions of ϕ.

The spectrometer collimator was placed along the centerline of the main flame. A preliminary scan of four data points was performed to determine the optimal collimator position with respect to its height above the burner surface. Given any potential uncertainty with respect to NH_2* emissions as a result of the 400 – 900-nm broadband observed in literature during NH_3-based combustion, the intensity trends of only NO*, OH*, and NH* were used during this preliminary calibration process. The following graphs of integrated intensities as functions of collimator height were developed:

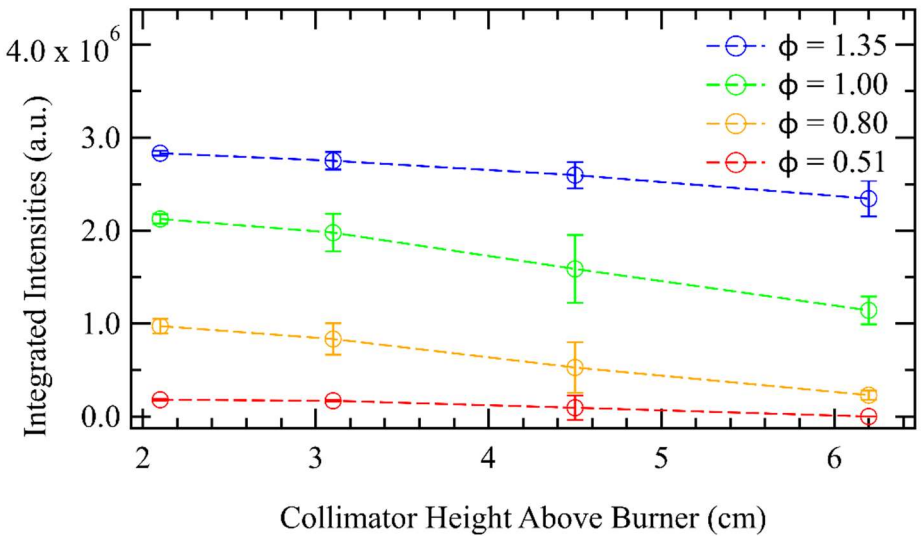

Figure 3.5 NO* background-removed integrated intensity as a function of collimator height for various key equivalence ratios.

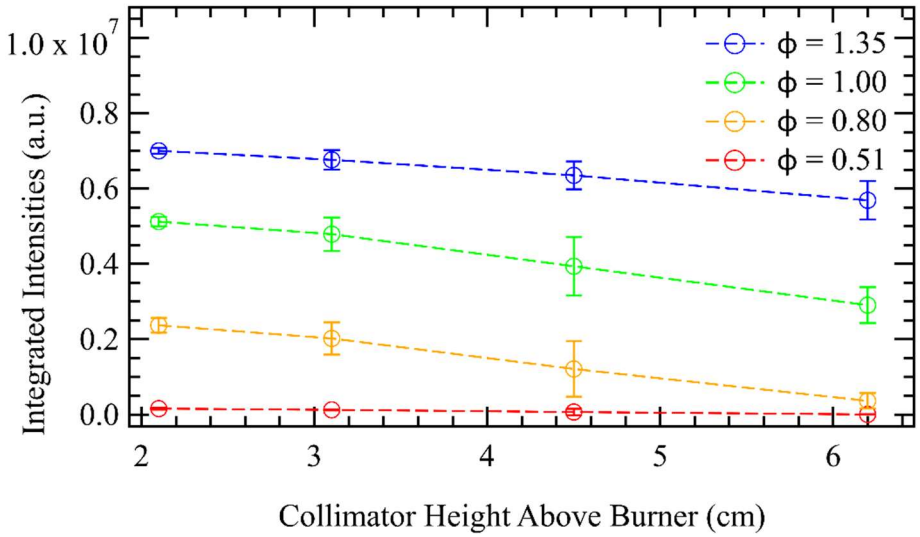

Figure 3.6 OH* background-removed integrated intensity as a function of collimator height for various key equivalence ratios.

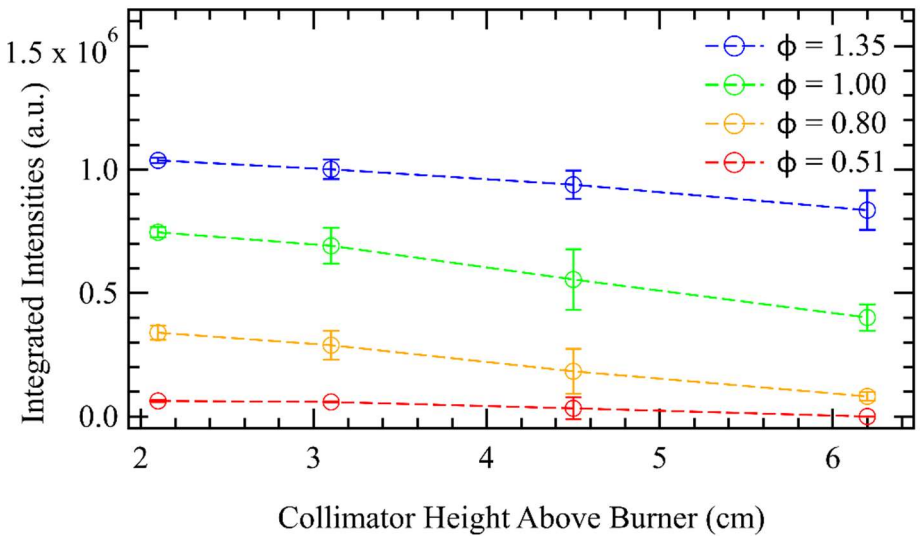

Figure 3.7 NH* background-removed integrated intensity as a function of collimator height for various key equivalence ratios.

For each of the three plots, the data was averaged over three repeated observations at the same experimental conditions. The error bars represent the 95% confidence interval (or two standard deviations in both directions). Physically, it was observed during this calibration that prior to 2 cm, the collimator's field of view was obstructed by the pilot flame. At 2 cm, the collimator height was sufficient to exceed that of the pilot flame, while at roughly 3 cm the collimator field of view was well above the pilot. By the time the collimator was 4 cm above the burner, its field of view had begun to exceed that of the main flame, and at 6.25 cm the collimator was consistently too high for most of the flame conditions tested. This observation is reinforced by the spectral trends seen in figure 3.5 – figure 3.7 as well. The signal intensities for all three excited species uniformly increased with ϕ. As the collimator height increased, the intensities of all species decreased, likely due to distance from the main reaction zone of the main flame yielding lower species densities. In general, the standard deviation of all three species across all ϕ was lowest at 2 cm. At this point, the collimator's field of view was as close to the reaction

zone of the main flame as possible without being obscured by the pilot flame. Once reaching a height of 3 – 4.5 cm, all species saw a steep rise in standard deviation. These heights increasingly became insufficient to capture the combustion events, especially for the short flames produced during lean conditions of ϕ below 0.6. As such, intermittently missing the area of greatest emission intensity yielded an increase in standard deviation. At 6.25 cm, the collimator was too high to detect the main flame behaviors of most of the tested conditions except for the exceptionally tall stoichiometric and rich flames. The standard deviations were therefore minimal since the majority of emissions were overlooked. These results indicate that, for the given experimental setup, the optimal collimator height to minimize signal variation, avoid pilot obstruction, and prevent missing the main flames was roughly 2 cm from the burner surface.

3.4. Chemiluminescence Imaging

OH* chemiluminescence images were collected using a Photron Fastcam SA-Z camera accompanied by a LaVision HS-IRO unit set at 50% gain. A 0.5 ms gate width and 1 kHz sampling frequency captured a total of 200 frames, each spanning 1024 × 1024 pixels. To convert to distance units, a scale was placed at the centerline of the burner and a calibration image was collected, obtaining a 130 pixels per cm resolution (or a total image area of 7.87 × 7.87 cm). Attempting to isolate the OH* emissions, a 50 mm diameter Semrock 315 nm ± 7.5 nm bandpass filter was used. This filter, which allows around 80% – 90% signal transmittance in the visible-IR region, has commonly been used in hydrocarbon OH* chemiluminescent studies given the lack of significant broadband emissions beyond 500 nm (as demonstrated in figure 3.4). However, the inclusion of NH_3 in this work's fuel blend resulted in considerable broadband emissions occuring within the transmission region of the 315 nm bandpass filter, as is shown in figure 3.8.

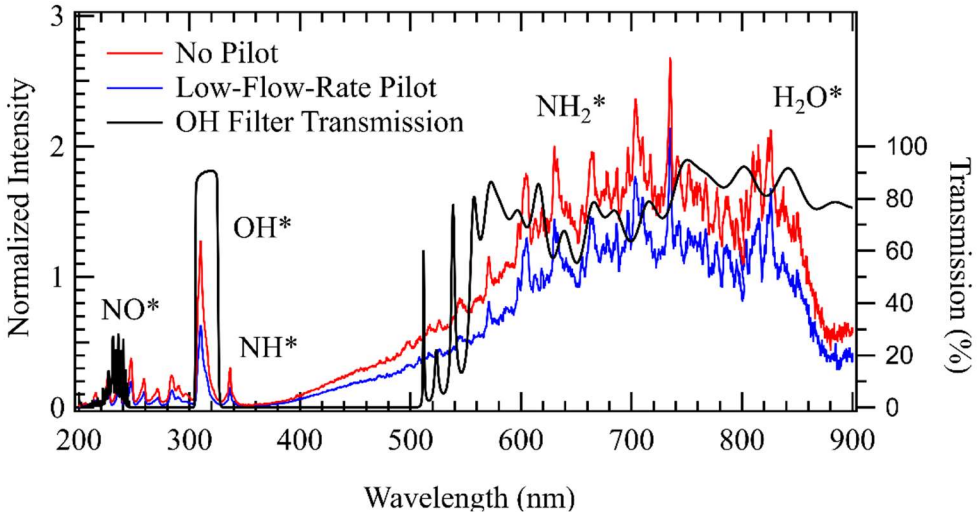

Figure 3.8 Overlap of OH filter transmission region and NH_3-blend spectra in the broadband region. NH_3-blend spectra were taken from the no pilot $\phi = 1.35$ and low-flow-rate pilot $\phi = 1.35$ cases and have been corrected for system quantum efficiency. For comparison, the spectra have been normalized with respect to the greatest OH peak encountered for the low-flow-rate pilot case at $\phi = 0.90$.

Given time constraints, additional filtration to remove the broadband transmittance could not be accomplished. In the results section, the outcome of OH* imaging and OH* spectrographic integration were compared as an attempted method of qualitatively assessing the extent of broadband interference.

In addition to the raw OH* imaging data, three backgrounds were collected (without the main NH_3-blend flame present): one without the pilot flame for those datasets collected before pilot introduction, one featuring the low-flow-rate pilot, and one featuring the high-flow-rate pilot. For the pilot backgrounds, 10 SLM of non-reactive N_2 was directed through the central channel to obtain a realistic expectation of the pilot profile. All backgrounds were obtained at the same intensifier gain, gate width, and sampling frequency as the raw OH* imaging data. The respective backgrounds were then averaged across the 200 collected frames and subtracted from

the appropriate OH* imaging data. Finally, the background-corrected OH* chemiluminescence images were averaged across all 200 frames and integrated to obtain plots of total OH* chemiluminescent intensity within the main flame as a function of ϕ. The integration area was chosen to capture the center of OH* production in the premixed main flame, while aiming to minimize the inclusion of the outer diffusion region. The same integration area was utilized for all pilot flames and ϕ cases for consistency. Figure 3.9 illustrates an example of this background subtraction and integration process for the high-flow-rate pilot, ϕ = 0.58 flame. It should be noted that the chemiluminescence images depict the sum total of OH emissions collected along the entire depth of the flame, and so do not provide planar resolution of OH* emissions.

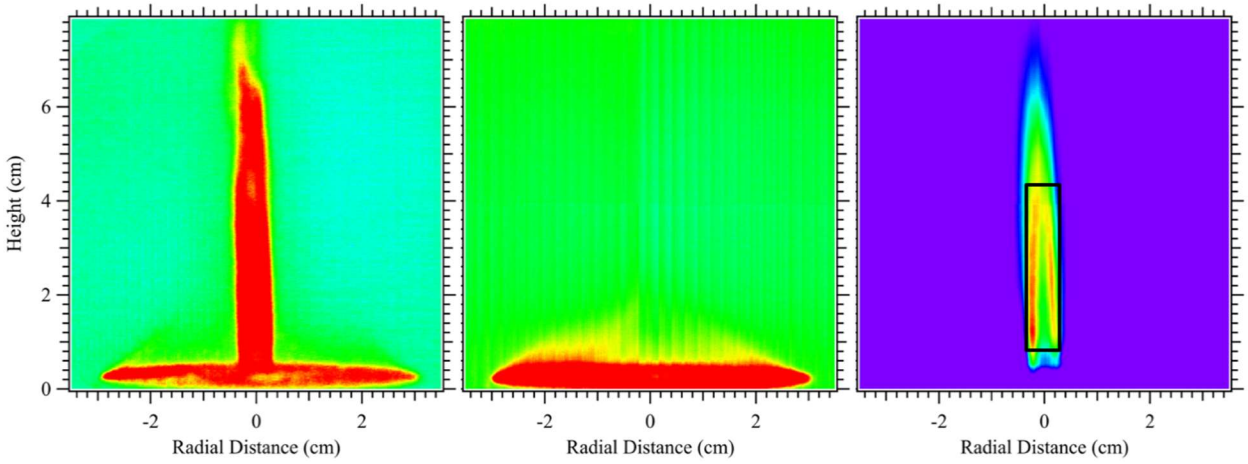

Figure 3.9 Sample OH* imaging background subtraction process for the high-flow-rate pilot flame at ϕ = 0.58 (From left to right): raw OH* frame with pilot and main flames; averaged OH* background with pilot flame only; and averaged OH* signal with pilot backgrounds subtracted and representative integration square overlayed.

4. RESULTS AND DISCUSSION

4.1. Visual Characterization Results

The results of the visual characterization were as follows. Without the influence of the pilot flame, the main flame was largely laminar. The addition of NH_3 to the flame produced a clearly visible layered cone structure, as opposed to the largely invisible appearance typical of H_2 combustion. Starting at 1.35, the ϕ of the main flame was lowered. A lean blowout limit was encountered when ϕ of 1.1~1.2 was reached. This blowout would occur either instantaneously, or after a few seconds. The flame was then reignited at the previously stable ϕ of 1.35. The introduction of the low-flow-rate, stoichiometric pilot flame resulted in immediate morphological changes in the main flame: the laminar behavior turned turbulent, with mixing in the outer layer obscuring the clearly defined conical layer previously observed. The pilot flame flow rates in this condition were H_2-2.0 SLM and air-4.76 SLM. At these flow rates, the pilot flame itself was largely invisible. The interaction of the pilot and main flames seemed to cause the main flame to lift off the surface of the burner, evident by the now-darker region around the base of the main flame. OH* chemiluminescence imaging was later used to confirm this. After pilot introduction, ϕ of the main flame was further decreased; as the flame grew leaner, increased turbulence caused the faint cone became entirely indetectable, and the brightness and height of the flame gradually decreased. When reaching ϕ of 0.6 ~ 0.7, the lack of fuel compared to the high air flow rate resulted in unburnt air avoiding the flame reaction zone and forming intermittent gaps and discontinuities in the flame. At ϕ of 0.58, the main flame once again became unstable, with the discontinuities consistently present rather than appearing sporadically. These observations are shown in figure 4.1.

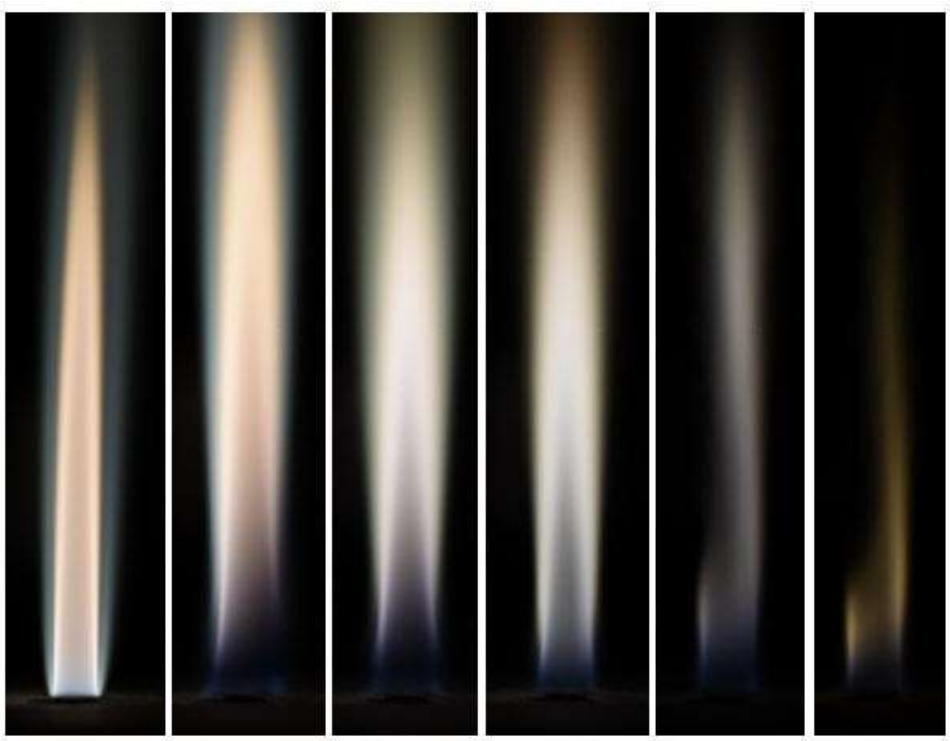

Figure 4.1 NH_3 flame behavior before and after low-flow-rate pilot flame introduction (from left to right): ϕ = 1.35 no pilot, and with the pilot on at ϕ = 1.35, 1.0, 0.70, 0.60, and 0.58.

At this point, the high-flow-rate pilot flame was introduced (H_2-4.0 SLM and air-9.52 SLM), yielding a second resurgence in flame stability. Immediately, the visibility of the main flame improved, and the discontinuities disappeared. Notably, the visibility of the pilot flame was also significantly increased, with a clear boundary forming between the pilot and the base of the main flame. The ϕ could however only be slightly decreased beyond this point, with the addition of further excess air rather quickly dampened the flame height and brightness once again. Once the ϕ was lowered below 0.5, the discontinuities remanifested dramatically: instead of intermittent gaps forming, the entire tip of the flame was cut off. This behavior is shown in figure 4.2.

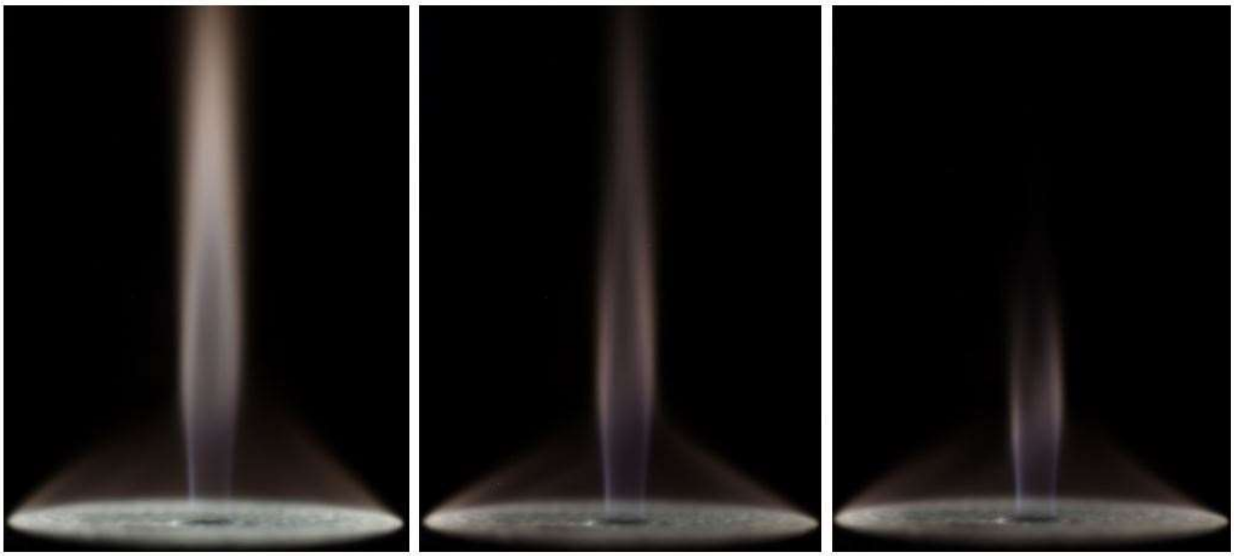

Figure 4.2 Piloted NH_3 flame behavior after the introduction of the high-flow-rate pilot flame (From left to right): ϕ = 0.58, 0.51, and 0.49.

4.2. Emission Spectroscopy Results

Spectroscopic analysis of the NH_3 flames revealed the effects of not only changing ϕ, but also the effect of the pilot flame via the background-removed spectra and integrated emission intensities. At the ϕ = 1.35 case when the low-flow-rate pilot flame was introduced. Since the orange color of the main flame was due to the broadband emitting over the visible range, which in turn was caused by the addition of NH_3 into the reacting mixture, the dilution of the reactant mixture by introduction of the low-flow-rate pilot flame diminished the luminous intensity of the main flame. This resulted in a slight decline in the overall spectral emission intensity. Additionally, turbulent mixing likely also played a role in the observed lowering of spectral intensity. These findings are shown in figure 4.3.

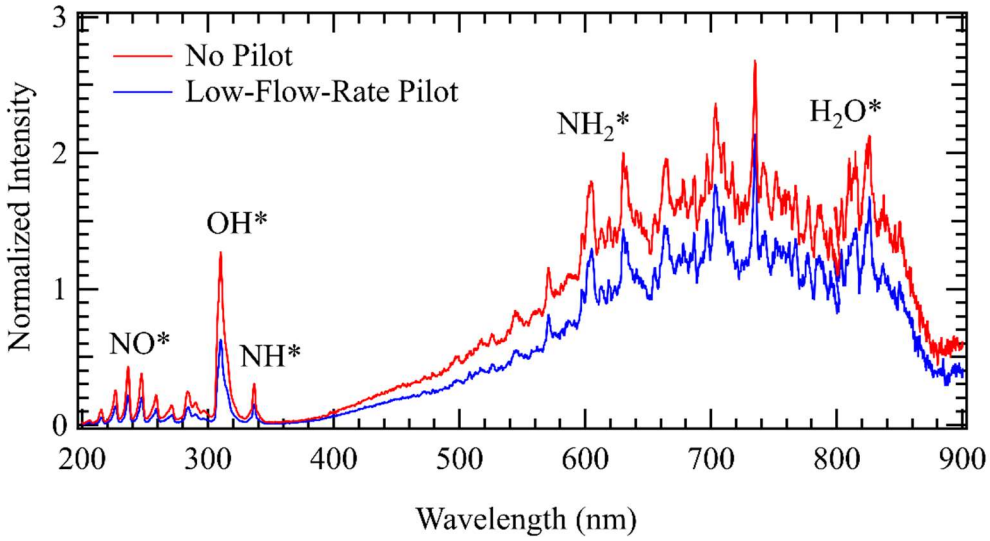

Figure 4.3 A sample background-removed spectra showing the effect of introducing low-flow-rate pilot flame in the $\phi = 1.35$ main flame. The spectra have been normalized with respect to the greatest OH peak encountered for the low-flow-rate pilot case at $\phi = 0.90$.

Figure 4.4 demonstrates the ϕ-dependent spectral behavior of the main flame for the low-flow-rate pilot case. The spectra shown have been normalized with respect to the greatest OH* peak encountered at $\phi = 0.90$. In general, the emission intensities are seen to decrease with ϕ, with further analysis of the species-specific trends ongoing.

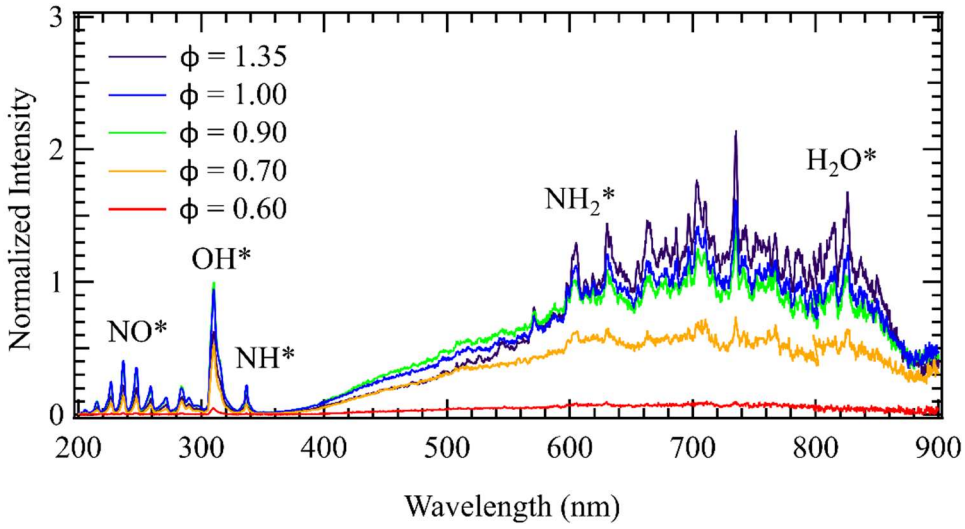

Figure 4.4 Spectral behavior of the main flame for the low-flow-rate pilot case as a function of ϕ. Rich to lean conditions tested. Spectra shown have been normalized with respect to the greatest OH peak encountered for the low-flow-rate pilot case at ϕ = 0.90.

A plot of NO*, OH*, NH*, and NH_2* integrated intensities versus ϕ for the low-flow-rate pilot case was generated and is shown in figure 4.5. All species indicate an increasing intensity with ϕ up to 1.35 and a stepwise decrease in integrated intensity after the introduction of the low-flow-rate pilot flame.

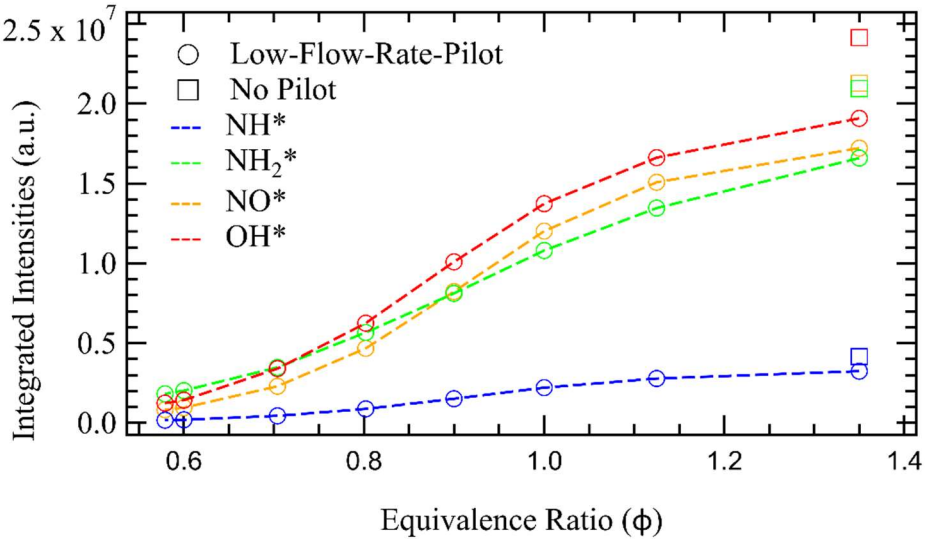

Figure 4.5 Background-removed integrated emission intensities of key species for the no pilot and low-flow-rate piloted flames.

At the $\phi = 0.58$ instability region, increasing the pilot flow rate produced a marked increase in the emissions of all key species, as well as the broadband emission seen between 350 – 900 nm and the H_2O emissions between 700 – 900 nm (figure 4.6). Despite the relative increase in intensities between the low- and high-flow-rate pilot cases, the overall signal strength of these lean conditions could not be returned to the intensity magnitudes previously seen for near stoichiometric and rich combustion conditions.

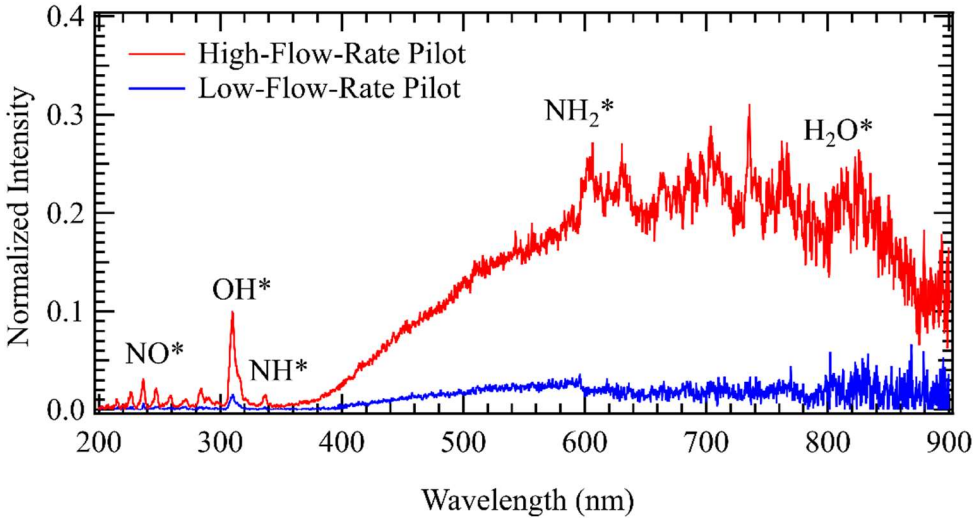

Figure 4.6 Effect on flame spectra of doubling the pilot flame flow rate. The spectra shown were recorded in the $\phi = 0.58$ flame and have been normalized with respect to the greatest OH peak encountered for the low-flow-rate pilot case at $\phi = 0.90$.

The instability of the main flame at these low ϕ caused the emissive intensity of the spectra to diminish exponentially as leaner conditions were reached (figure 4.7). At $\phi = 0.46$, the spectral lines of the key species was barely distinguishable above the background.

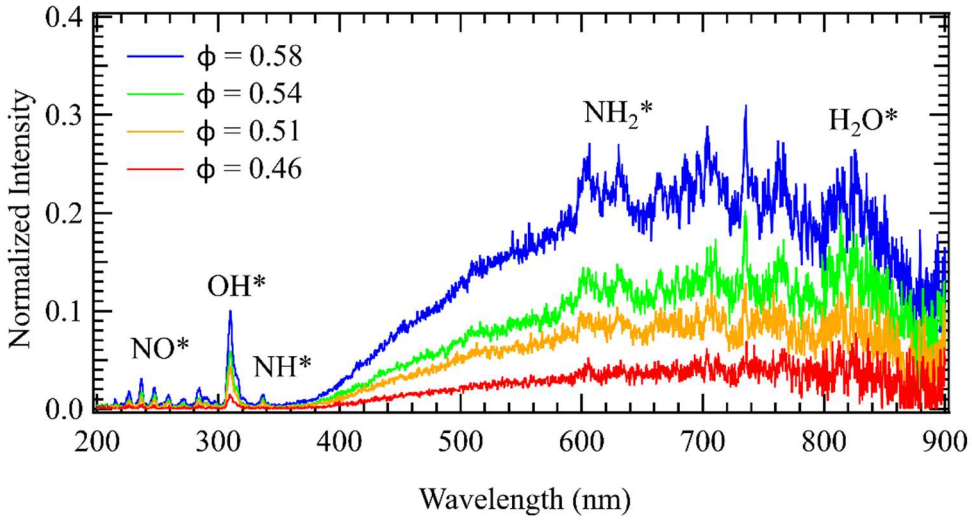

Figure 4.7 Spectral behavior of the main flame for the high-flow-rate pilot case as a function of ϕ. Lean conditions tested. Spectra shown have been normalized with respect to the greatest OH peak encountered for the low-flow-rate pilot case at ϕ = 0.90.

Notably, although the spectra indicated an increase in intensity after introducing the high-flow-rate pilot, the integrated intensities before and after introduction were roughly the same. The factors causing the declining species intensities continued into these lower ϕ ranges, as seen in figure 4.8. As was discussed previously with respect to the visual characterization, the increased pilot flow rate only produced a limited improvement in the main flame stability. The integrated intensities of the remaining NH_2*, NO*, and OH* signals continued to drop exponentially as ϕ was decreased, while the NH* signals dwindled more gradually given their already low values. After ϕ = 0.46, with the main flame barely distinguishable above the pilot, no significant OH*, NH_2*, NH*, or NO* integrated intensities could be detected.

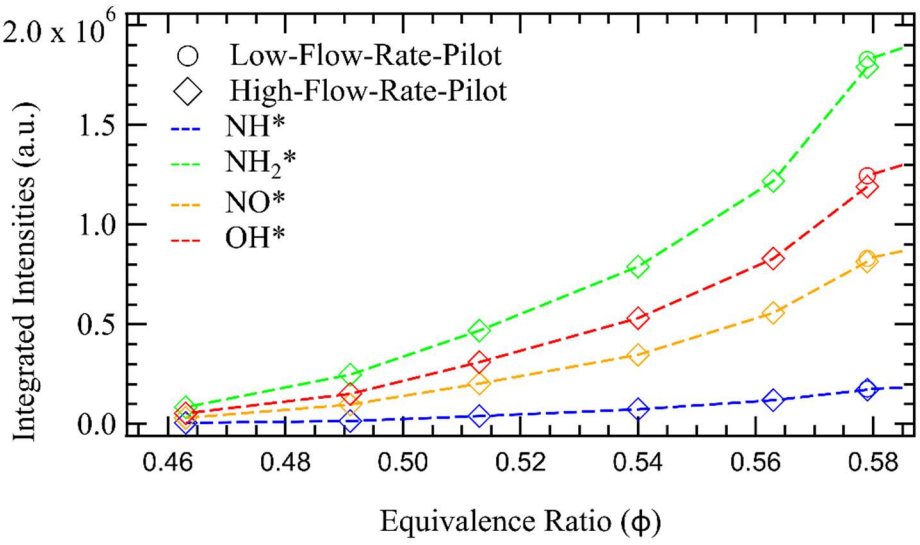

Figure 4.8 Background-removed integrated intensities of key species for the low- and high-flow rate piloted flame cases.

In order to estimate the lean blowout limit of the main flame, ϕ was gradually lowered until reaching an extremely lean 0.16. With a boundary and some NH_3-blend combustion still visible between the main and pilot flames, the NH_3 and H_2 supplies were shut off. Without these species, the main flame grew noticeably fainter (figure 4.9). Since no key species emissions were detectable beyond ϕ = 0.46 equivalence ratio, it was not possible to spectrally confirm the existence or the composition of the main flame at this point. The visual results led to the hypothesis that a form of pilot/main flame interaction may either be preventing the main flame from blowing out or preventing the blowout limit from being detected. The OH* chemiluminescence imaging diagnostics were used to better detect potential blowout behavior, since this technique offered information regarding spatial distributions of species not available using the spectral emission results.

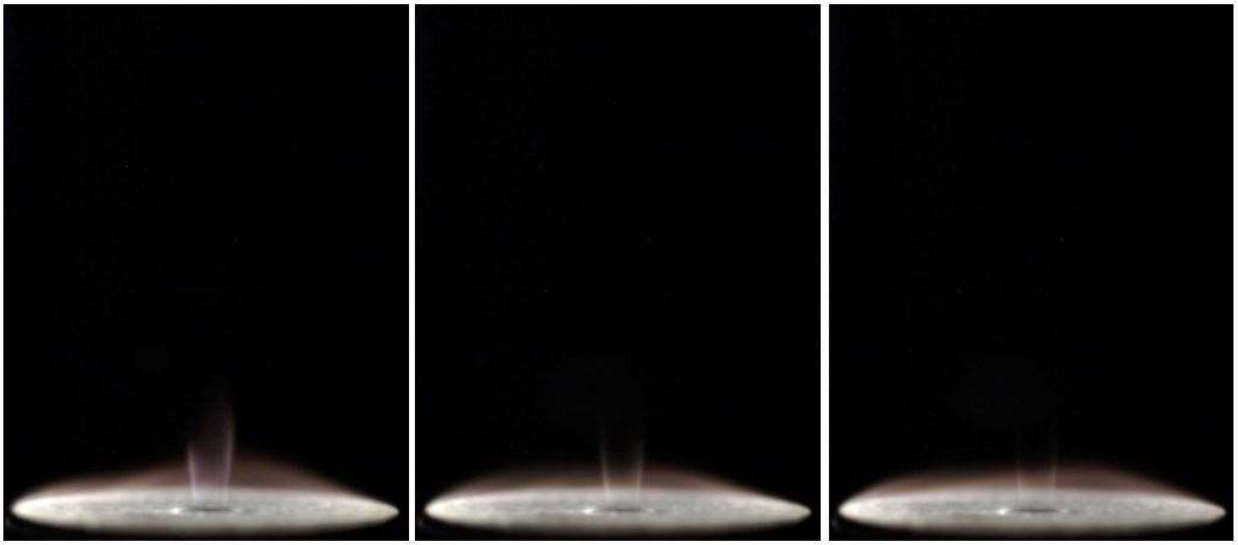

Figure 4.9 High-flow-rate pilot flame under extremely lean conditions (From left to right): ϕ = 0.16 ammonia blend; NH_3 shut off, only H_2 and N_2 in main flame; NH_3 and H_2 shut off, only air and N_2 flowing through the central tube. Image brightness was increased by 50% for all cases to aid visibility.

4.3. Chemiluminescence Imaging Results

The OH* chemiluminescence imaging was able to provide additional insight into the interactions of the main and pilot flames, the emission spectroscopy results, and the observed main flame behavior at extremely lean ϕ.

Figure 4.10 depicts the flame both before and after introducing the low-flow-rate pilot flame. At ϕ = 1.62 before pilot introduction, the flame was observed to flicker occasionally, resulting in the outer diffusion area of the flame producing an elongated, lopsided profile after averaging across all collected frames. The central area of highest OH* intensity was used as a means of locating the reaction zone of the main flame [7]. Given the previously addressed inability to reach stoichiometric conditions unpiloted, the low-flow-rate pilot flame was introduced at ϕ = 1.35 and immediately resulted in a distinct shift in the morphology of the flame

and the location of the reaction zone. The reaction zone of the main flame is seen to lift off the burner, confirming the speculations made during qualitative visual analysis. At $\phi = 1.0$, the flame lifting had slightly decreased.

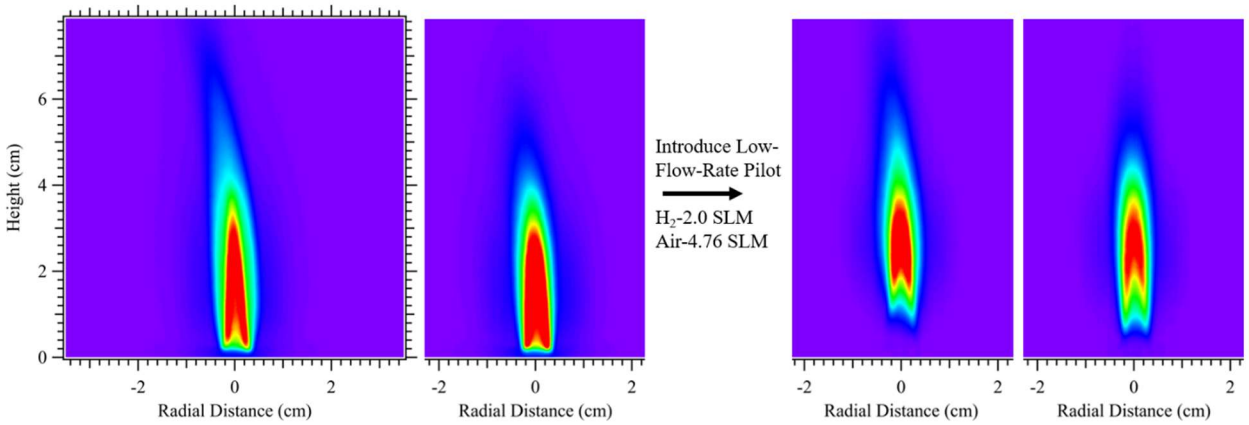

Figure 4.10 OH* imaging effect of introducing low-flow-rate pilot flame (From left to right): $\phi = 1.62$ no pilot, $\phi = 1.35$ no pilot, and with the pilot on at $\phi = 1.35$ and $\phi = 1.00$.

Figure 4.11 and figure 4.12 show that, as the ϕ of the main flame was lowered, the reaction zone of the main flame was seen to grow noticeably fainter after $\phi = 0.8 \sim 0.7$. This offered some explanation for the intermittent flame discontinuities and gaps observed during visual analysis. For figure 4.12 and onward, due to the quickly deteriorating chemiluminescent intensities, the flame intensity scales were increased fourfold to allow for better visualization. With a diminishing reaction zone at progressively leaner conditions, the likelihood of reactant air not undergoing combustion increased. By $\phi = 0.58$, the pilot reaction zone had dwindled considerably, likely causing the consistent gaps witnessed during qualitative visualization.

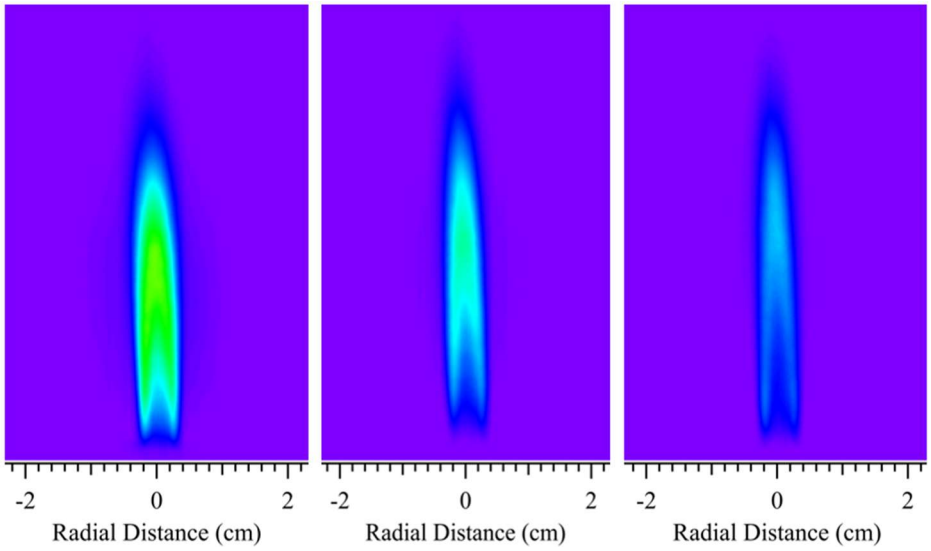

Figure 4.11 OH* images of increasingly lean low-flow-rate piloted flames (From left to right): ϕ = 0.80, 0.70, and 0.65.

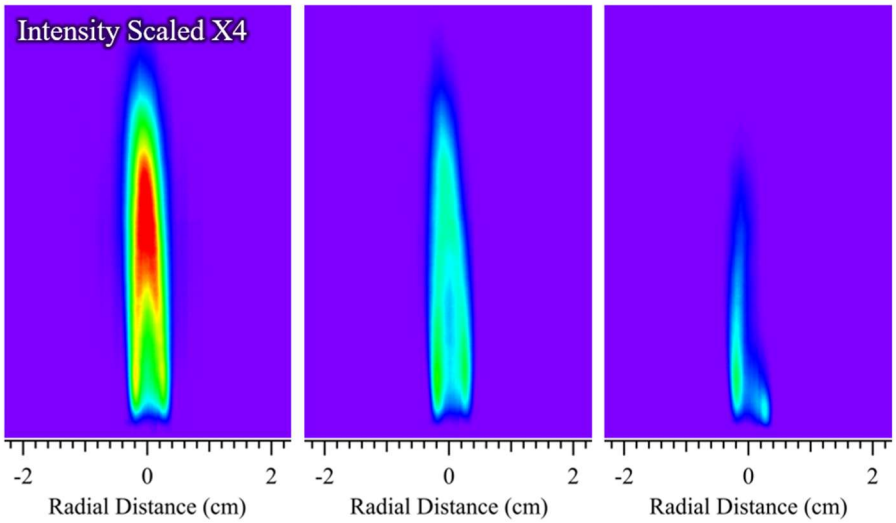

Figure 4.12 OH* images of increasingly lean low-flow-rate piloted flames (From left to right): ϕ = 0.65, 0.60, and 0.58. All image intensity scales have been increased fourfold to improve visibility.

For the imaging study, a comparison was made between introducing the high-flow-rate pilot at ϕ = 0.6 and at ϕ = 0.58 (figure 4.13). When introduced at the more stable ϕ = 0.6 the main flame height improved slightly. A significant resurgence in the reaction zone was also

observed. In comparison, when introduced at the ϕ = 0.58 stability limit, a more drastic improvement in the flame height occurred, though the flame reaction zone predictably did not recover to the same extent. Neither case seemed to demonstrate an increase in the main flame lifting behavior as had been observed during the introduction of the low-flow-rate pilot. The remaining imaging analysis was done with respect to initiating the high-flow-rate pilot flame at ϕ = 0.58.

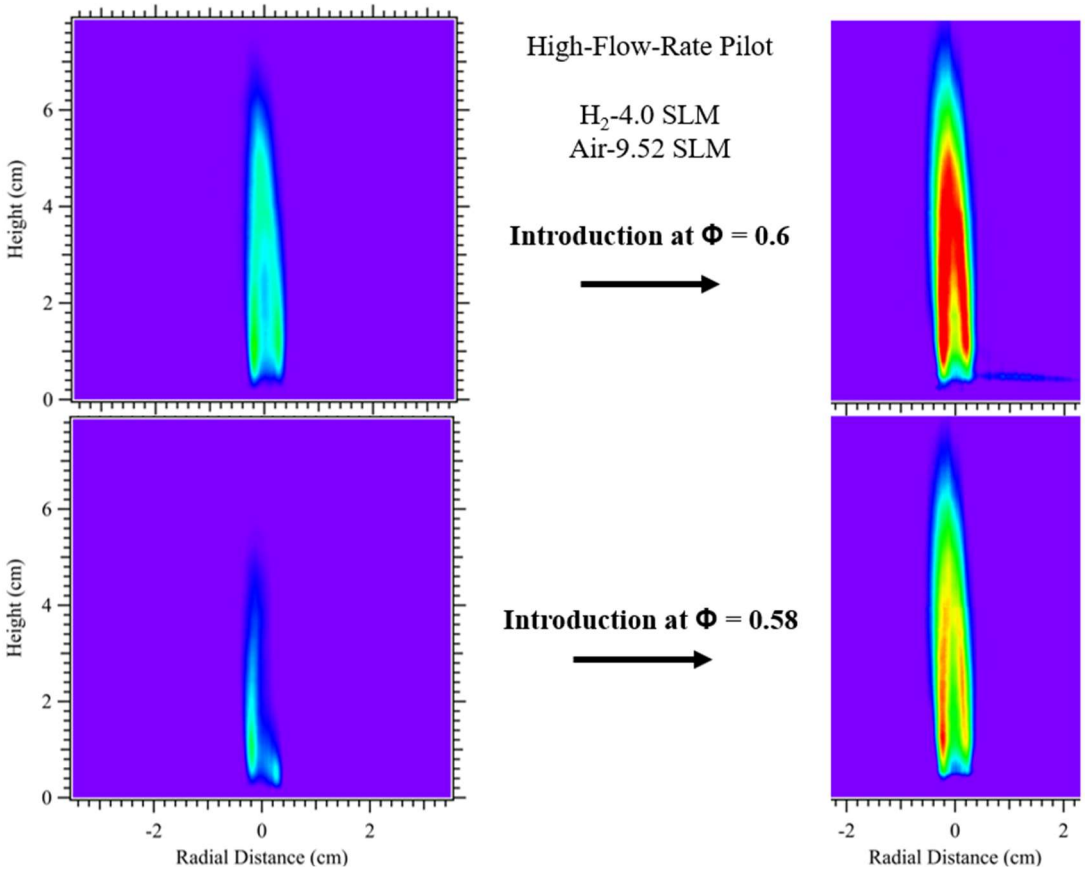

Figure 4.13 OH* imaging effect of introducing the high-flow-rate pilot flame at different ϕ (top left, top right, bottom left, bottom right): ϕ = 0.6 flame with low-flow-rate pilot, ϕ = 0.6 flame with high-flow-rate pilot, ϕ = 0.58 flame with low-flow-rate pilot, and ϕ = 0.58 flame with high-flow-rate pilot. All image intensity scales have been increased fourfold to improve visibility.

The spatial resolution of the OH* imaging results provided previously unavailable insight into the causes for the exponential decrease in flame stability once reaching ϕ below 0.58. Figure 4.14 and figure 4.15 demonstrate a sharp decline in flame height. Moreover, starting at ϕ = 0.58, an area of decreasing OH* chemiluminescent intensity along the centerline of the main flame was observed. Finally, at ϕ = 0.40, there was almost no OH* visible in the main flame. The loss of OH* along the flame centerline explains the exponential decline and eventual inability to detect key species emissions above the background for ϕ below 0.46 during spectroscopic emission analysis, since this measurement had been taken at a single point along the centerline of the flame.

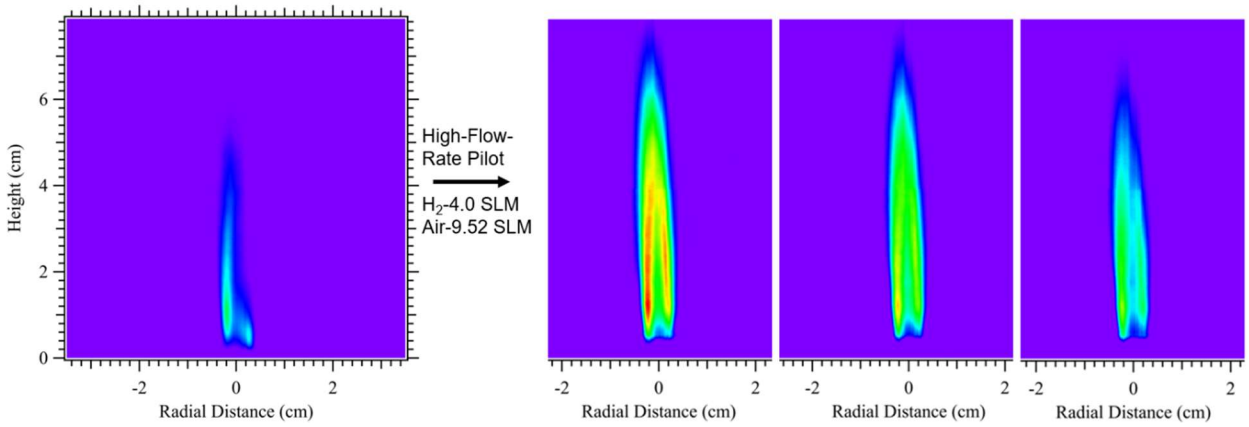

Figure 4.14 OH* imaging effect of introducing high-flow-rate pilot flame (From left to right): ϕ = 0.58 low-flow-rate pilot, and with the high-flow-rate pilot on at ϕ = 0.58, 0.56 and 0.54. All image intensity scales have been increased fourfold to improve visibility.

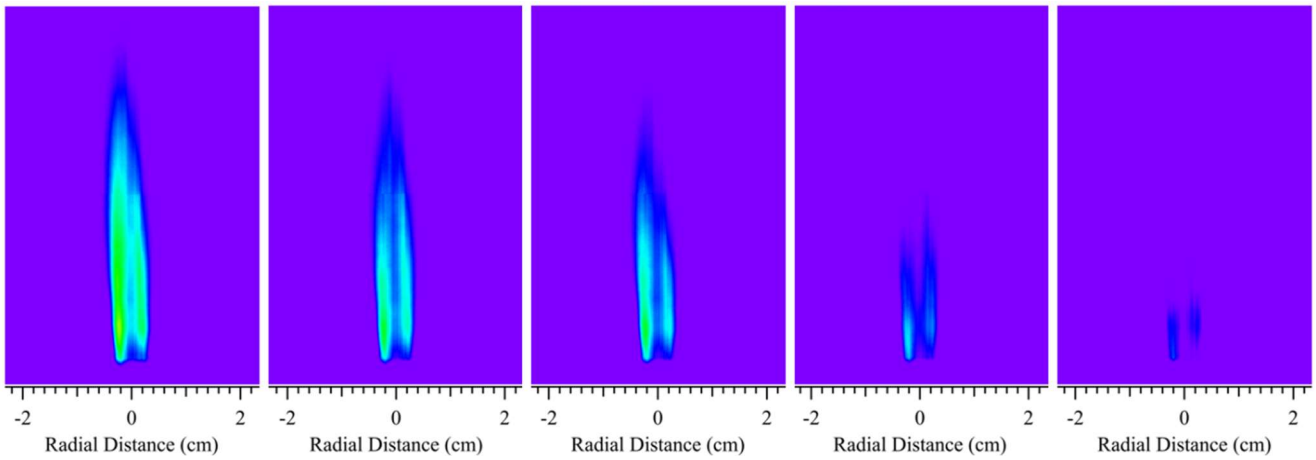

Figure 4.15 OH* images of increasingly lean high-flow-rate piloted flames. (From left to right): ϕ = 0.54, 0.51, 0.49, 0.46, and 0.40. All image intensity scales have been increased fourfold to improve visibility.

The following discussion compares the OH* imaging results with that of the spectral emission analysis as an attempted method of qualitatively assessing the extent of broadband interference in the OH* imaging data. The spectra obtained during emission analysis, with the ability to select which wavelength regions to integrate, prevented contamination of the OH* signal by the broadband or other species in close spectral proximity. To compare these results with that of the OH* imaging technique, additional spectral scaling needed to be done to account for the OH* imaging technique's Photron camera and HS-IRO unit spectral sensitivities. Figure 4.16 depicts the OH* imaging system's total efficiency curve as the product of its camera and intensifier unit sensitivities.

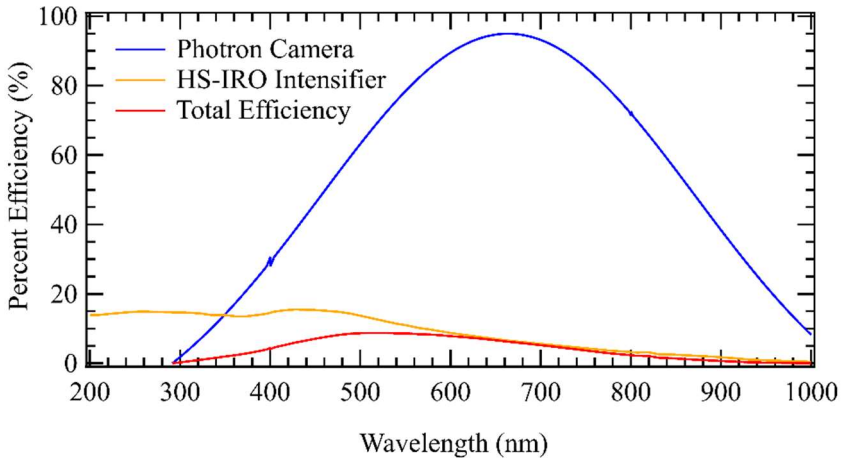

Figure 4.16 OH* imaging setup's Photron camera, intensifier unit, and total efficiency curves as functions of wavelength.

After scaling, the spectral emission data were integrated along the FWHM range of the OH* band and the range of broadband transmission through the OH filter (500 nm - 900 nm). The sum of these two integrated intensities was then compared to the integrated OH* imaging results (figure 4.17). A similar exponential decline as a function of equivalence ratio is observed for both. However, the spatial integration of the OH* imaging results meant that the resurgence observed after low- and high-flow-rate pilot introduction yielded an increase in OH* intensity, in comparison to the stepwise decrease observed for the point integrated spectra intensities. Beyond these observations, it was not possible to compare the effect of broadband interference on the OH* imaging results further. As such, only qualitative conclusions could be drawn with respect to flame behavior from the imaging data.

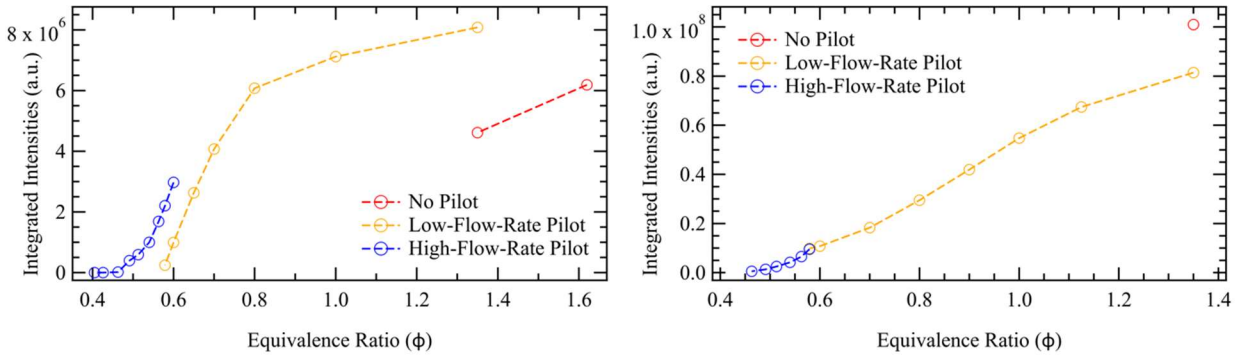

Figure 4.17 Trend comparison: integrated OH* imaging data (left), integrated OH* + broadband spectral emissions (right). Integrated OH* + broadband signal has been adjusted to account for the OH* imaging equipment's spectral response.

When introducing the low-flow-rate pilot flame, the integrated OH* chemiluminescent signal is observed to increase as a result of the spatial integration method used and the flame reaction zone resurgence produced by the pilot. As the ϕ was lowered the intensity decreased, with accelerated decline occurring once the ϕ = 0.7 ~ 0.8 instability region was passed. Upon introducing the high-flow-rate pilot flame, another stepwise improvement occurred. The continued decreasing of the main flame ϕ further lowered the OH* chemiluminescent intensity, eventually remaining consistent at roughly zero for ϕ below about 0.45.

The lifting observed after low-flow-rate pilot introduction in the OH* imaging results may be explained by the previously addressed numerical and experimental findings of [19]. With respect to pilot temperature effects, the temperature of the stoichiometric H_2-air pilot flames were expected to be consistently greater than those of the $H_2/NH_3/N_2$-air pilot flame, improving the flame speed due to localized decreases in mixture density. However, given the lifting effects observed once the low-flow-rate pilot was introduced, it is clear that the laminar flame speed was decreased. The effect of pilot composition addressed by [19] clarifies this. A product of pilot/main flame mixing, the region formed by the main flame diffusion area and hot pilot gases

(i.e., the “pilot reaction zone”) was found to have lower reaction and diffusion rates than that of the pure main flame. As such, the decrease in the main flame’s reaction and diffusion rates likely outweighed any density benefits caused by thermal effects. Given the lack of planar resolution available using the OH* imaging technique, it was not possible to confirm whether the central axis of the pure, unmixed main flame was lifted as well.

The effects of pilot/main flame mixing and forming a secondary pilot reaction zone are also possible explanations of the gradual loss of the OH* chemiluminescence along the main flame centerline and decline of OH* imaging integrated intensity with leaner ϕ. According to [19], the level of pilot/main flame mixing increased when the difference between the two flame’s ϕ grew larger, with the resultant pilot reaction zone ϕ being greater than that of the main flame when burning at lean conditions. This would help sustain the main flame at ϕ previously below the flammability limit and was likely the mechanism responsible for allowing the main flame to reach lean ϕ once the pilot was introduced in the current work. Doubling the flow rate of the pilot to the high-flow-rate case yielded a resurgence in main flame stability and OH* production possibly due to increased turbulent mixing between the two flames. At ϕ of 0.58 and below, the outer diffusion region of the main flame involved in forming the pilot reaction zone likely represented an increasing portion of the NH_3-blend combustion reaction. By $\phi \sim 0.40$, there was no OH* detectible in the inner main flame reaction zone, with all OH* production localized in the pilot reaction zone. It is therefore determined that the main flame reaction zone of the 40% H_2, 45% NH_3, 15% N_2 blend under the present experimental conditions had been extinguished at $\phi \sim 0.40$, with only the pilot reaction zone remaining. This reaction zone would therefore be the result of hot gases supplied by the pilot undergoing combustion with the main flame reactants, as opposed to the mixing of the hot gases with the now-extinct main flame diffusion region.

The insight provided by the OH* imaging results provides some clarification of the flame behavior at extremely lean conditions, when during emission spectroscopy the ϕ was lowered to 0.16 and the NH_3 and H_2 supplies were cut off. With the main flame reaction zone extinguished by $\phi = 0.40$, the sole remaining reaction zone responsible for NH_3-blend combustion the pilot flame reaction zone. With the excessive main flame airflow, relative lack of NH_3, and the pilot reaction zone mainly containing H_2, the faint nature of the main flame is expected. Once the main flame NH_3 and H_2 were removed, the remaining combustion events were likely caused by the pilot reaction zone's H_2 supply and main channel's airflow, with the resultant flame being near invisible.

For comparison of the obtained experimental data to numerical approximations, preliminary Cantera simulations were created using the GRI 3.0 chemical kinetics mechanism. The number densities of numerous key species and the adiabatic flame temperature of the $NH_3/H_2/N_2$-air blend were estimated as functions of equivalence ratio (figure 4.18). These predictions were performed for equilibrium NH_3-blend combustion, so the trends formed likely differ from the expected experimental behavior since the influence of the pilot flame and turbulent mixing effects could not be accounted for. Additionally, without calibration, it is not possible to directly relate spectral emission intensity to number density or other quantitative measures of species concentration. The trends could however provide an estimate of the general behavior of the NH_3-blend. Predictably, the adiabatic flame temperature would be maximized around stoichiometry, and the O_2 number density would increase exponentially as a function of ϕ. The trends formed by the other key species indicate the same exponential decrease with ϕ as was obtained during the current study; however, a maximizing behavior is observed by the simulation, followed by a steep drop just before or after surpassing stoichiometric ϕ. These

results are currently not replicated by the spectral emission and imaging results obtained, possibly due to broadband interference or other factors. Instead, the spectral emission and imaging results appear continuous after stoichiometric ϕ. Investigation into the trends observed and the effect of unintended broadband transmission are ongoing.

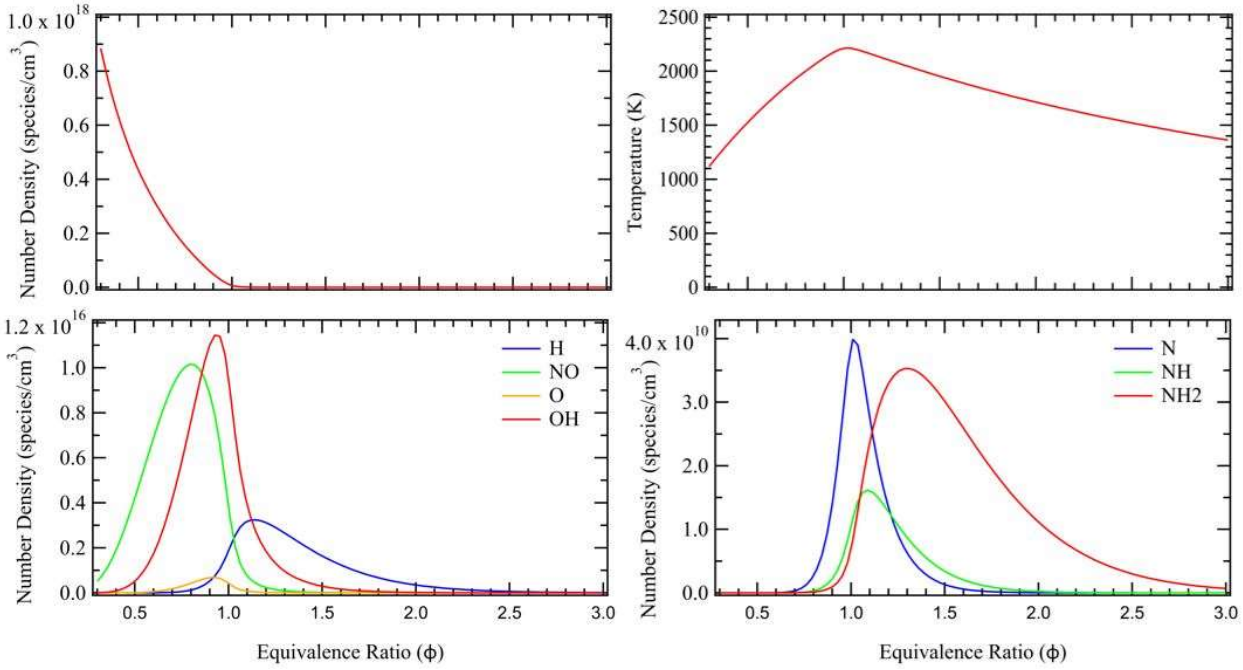

Figure 4.18 Simplified Cantera simulations as functions of ϕ (top left, top right, bottom left, bottom right): O_2 number density; adiabatic flame temperature; H, NO, O, OH number densities; and N, NH, NH_2 number densities.

5. CONCLUSIONS AND RECOMMENDATIONS

This work demonstrates the combustion behavior of premixed laminar, atmospheric-pressure, piloted $H_2/NH_3/N_2$-air combustion on a modified McKenna burner using qualitative visual characterization, spectral emission analysis, and high-speed OH* chemiluminescence imaging. The low-flow-rate pilot flame allowed the NH_3-blend combustion to reach stoichiometric and lean equivalence ratios where the flame would previously have blown out without the aid of the pilot flame. Furthermore, upon introduction of the pilot flame, turbulent mixing in the outer region of the flame was observed, as well as the main flame lifting from the burner surface. Burning at $\phi \sim 0.7$ or lower resulted in intermittent gaps forming within the main flame due to excessive airflow leaking around the diminishing main flame reaction zone. These gaps would remain consistently once $\phi = 0.58$ was reached.

Emission spectroscopy was able to provide trends of key species behavior as a function of equivalence ratio, namely NO*, OH*, NH*, and NH_2* chemiluminescence profiles. Lowering the ϕ resulted in exponentially declining species intensities. When burning at $\phi = 0.46$ or lower, no significant species emissions were detectable above the background. As such, the existence of the main flame could not be spectrally confirmed. Visually, the flame appearance did not significantly change between $\phi = 0.46$ and $\phi = 0.16$, even when the supplies of reactive NH_3 and H_2 in the fuel blend were cut off and only air and non-reactive N_2 were supplied through the main channel.

OH* chemiluminescence imaging was able to clarify the behaviors observed during qualitative visual characterization and emission spectroscopy analysis, particularly at the lower limits of the lean conditions tested. The main flame reaction zone tends to lift off the burner surface once the low-flow-rate pilot flame was introduced, though increasing the pilot flow rate

did not seem to further exacerbate this behavior. The reaction zone of the main flame quickly became faint when burning at $\phi \sim 0.8$ or lower, providing explanation for the instability demonstrated at this point. At $\phi = 0.46$, the main flame OH* production region had localized around the outer edges of the main flame, which was why no considerable key species emissions were detected during emission spectroscopy after $\phi = 0.46$. Furthermore, at $\phi = 0.40$, the OH* chemiluminescence of the main flame, and thus the main flame reaction zone, had likely extinguished. As a result, the pilot reaction zone remained the sole combusting event and was responsible for visually prolonging the flame up to $\phi = 0.16$.

One vital area for continued experimental improvement would be the prevention of broadband interference in the OH* imaging signal. Though the 315-nm OH bandpass filter used has been commonly applied in hydrocarbon OH* chemiluminescence imaging studies, the introduction of NH_3 fuel blend in the present work resulted in the emergence of a considerable broadband feature, which coincided with the neat-IR transmission range of the OH bandpass filter. Due to time constraints, additional filtration to prevent this broadband interference was not feasible during this study. Future work includes the addition of a shortpass filter to prevent chemiluminescence transmission above 500 nm, thereby preemptively avoiding the broadband interreferences present in NH_3 flames.

Further analytical efforts would include quantitative diagnostics of the main and pilot flame's turbulent intensities, burning velocities, heat release rates, and approximations of heat lost to the burner. Additionally, to avoid the interference of a varying total flow rate, the equivalence ratio scans should be repeated under constant total flow conditions. This result may be accomplished by adjusting the required ratios of fuel and air for a given equivalence ratio while keeping the sum of the reactant flows constant.

REFERENCES

[1] S.C. Anenberg, J. Schwartz, D. Shindell, M. Amann, G. Faluvegi, Z. Klimont, G. Janssens-Maenhout, L. Pozzoli, R. V. Dingenen, E. Vignati, L. Emberson, N. Z. Muller, J. J. West, M. Williams, V. Demkine, W. K. Hicks, J. Kuylenstierna, F. Raes, and V. Ramanathan, "Global air quality and health co-benefits of mitigating near-term climate change through methane and black carbon emission controls," *Environmental Health Perspectives*, vol. 120, no. 6, pp. 831–839, 2012.

[2] H. Lee and M. Lee, "Recent advances in ammonia combustion technology in thermal power generation system for carbon emission reduction," *Energies*, 14, no. 18, 2021.

[3] A. M. Elbaz, S. Wang, T. F. Guiberti, and W. L. Roberts, "Review on the recent advances on ammonia combustion from the fundamentals to the applications," *Fuel Communications*, vol. 10, 2022.

[4] Y. Jiang, A. Gruber, K. Seshadri, and F. Williams, "An updated short chemical-kinetic nitrogen mechanism for carbon-free combustion applications," *International Journal of Energy Research*, vol. 44, no. 2, pp. 795–810, 2019.

[5] S. Wiseman, M. Rieth, A. Gruber, J. R. Dawson, and J. H. Chen, "A comparison of the blow-out behavior of turbulent premixed ammonia/hydrogen/nitrogen-air and methane-air flames," *Proc. Comb. Inst.*, vol. 38, pp. 2869–2876, 2021.

[6] W. Weng, M. Aldén, and Z. Li, "Visible chemiluminescence of ammonia premixed flames and its application for flame diagnostics," *Proc. Combust. Inst.*, vol. 39, pp. 1–8, 2022.

[7] Q. Fan, X. Liu, L. Xu, A. A. Subash, C. Brackmann, M. Aldén, X. Bai, and Z. Li, "Flame structure and burning velocity of ammonia/air turbulent premixed flames at high Karlovitz number conditions," *Combustion and Flame*, vol. 238, 2022.

[8] D. Dirtu, L. Odochian, A. Pui, and I. Humelnicu, "Thermal decomposition of ammonia. N2H4 - an intermediate reaction product," *Open Chemistry*, vol. 4, no. 4, pp. 666–673, 2006.

[9] T. Mendiara and P. Glarborg, "Ammonia chemistry in oxy-fuel combustion of methane," *Combustion and Flame*, vol. 156, pp. 1937–1949, 2009.

[10] H. Kobayashi, A. Hayakawa, K. D. K. A. Somarathne, and E. C. Okafor, "Science and technology of ammonia combustion," *Proc. Combust. Inst.*, vol. 37, pp. 109–133, 2019.

[11] S. Mashruk, M. Kovaleva, C. T. Chong, A. Hayakawa, E. C. Okafor, and A.Valera-Medina, "Nitrogen oxides as a by-product of ammonia/hydrogen combustion regimes," *Chemical Engineering Transactions*, vol. 89, 2021.

[12] A. Alnasif, S. Mashruk, M. Kovaleva, P. Wang and A. Valera-Medina, "Experimental and numerical analyses of nitrogen oxides formation in a high ammonia-low hydrogen blend using a tangential swirl burner," *Carbon Neutrality*, vol. 1, no. 24, 2022.

[13] C. Lhuillier, P. Bréquigny, F. Contino, and C. Mounaïm-Rousselle, "Experimental study on NH3/H2/air combustion in spark-ignition engine conditions," *Hyper Articles en Ligne (HAL)*, 11th Mediterranean Combustion Symposium, 2019.

[14] O. Kurata, N. Iki, T. Matsunuma, T. Inoue, T. Tsujimura, H. Furutani, H. Kobayashi, and A. Hayakawa, "Performances and emission characteristics of NH3–air and NH3–CH4–air combustion gas-turbine power generations," *Proc. Combust. Inst.*, vol. 36, pp. 3351–3359, 2017.

[15] D. Lee and H. H. Song, “Development of combustion strategy for the internal combustion engine fueled by ammonia and its operating characteristics,” *Journal of Mechanical Science and Technology*, vol. 32, no. 4, pp. 1905–1925, 2018.

[16] O. Mathieu, E. L. Petersen, “Experimental and modeling study on the high-temperature oxidation of Ammonia and related NO_x chemistry,” *Combustion and Flame*, vol. 162, pp. 554–570, 2015.

[17] S. J. Klippenstein, L. B. Harding, P. Glarborg, J. A. Miller, “The role of NNH in NO formation and control,” *Combustion and Flame*, vol. 158, pp. 774–789, 2011.

[18] J. A. Miller and C. T. Bowman, “Mechanism and modeling of nitrogen chemistry in combustion,” *Progress in Energy and Combustion Science*, vol. 15, pp. 287–338, 1989.

[19] S. Yu, X. S. Bai, B. Zhou, Z. Wang, Z. S. Li, and M. Aldén, “Numerical studies of the pilot flame effect on a piloted jet flame,” *Combustion Science and Technology*, vol. 194, no. 2, pp. 351–364, 2022.

[20] C. Brackmann, V. A. Alekseev, B. Zhou, E. Nordström, P.-E. Bengtsson, Z. Li, M. Aldén, and A. A. Konnov, “Structure of premixed ammonia + air flames at atmospheric pressure: Laser diagnostics and kinetic modeling,” *Combustion and Flame*, vol. 163, pp. 370–381, 2016.

[21] A. Hayakawa, T. Goto, R. Mimoto, Y. Arakawa, T. Kudo, and H. Kobayashi, “Laminar burning velocity and Markstein length of ammonia/air premixed flames at various pressures,” *Fuel*, vol. 159, pp. 98–106, 2015.

[22] A. A. Khateeb, T. F. Guiberti, X. Zhu, M. Younes, A. Jamal, and W. L. Roberts, “Stability limits and NO emissions of technically-premixed ammonia-hydrogen-nitrogen-air swirl flames,” *International Journal of Hydrogen Energy*, vol. 45, pp. 22008–22018, 2020.

[23] X. Zhu, A. A. Khateeb, W. L. Roberts, and T. F. Guiberti, “Chemiluminescence signature of premixed ammonia-methane-air flames,” *Combustion and Flame*, vol. 231, 2021.

[24] A. Hayakawa, T. Goto, R. Mimoto, T. Kudo, and H. Kobayashi, “NO formation/reduction mechanisms of ammonia/air premixed flames at various equivalence ratios and pressures,” *Mechanical Engineering Journal*, vol. 2, no. 1, 2015.

[25] D. E. Paulsen, W. F. Sheridan and R. E. Huffman, “Thermal and recombination emission of NO2,” *The Journal of Chemical Physics*, vol. 53, pp. 647–658, 1970.

[26] R. W. B. Pearse and A. G. Gaydon*, The Identification of Molecular Spectra*, fourth edition, John Wiley & Sons, Inc., pp. 234, 1976.

[27] L. S. Rothman, I. E. Gordon, A. Barbe, D. C. Benner, P. F. Bernath, M. Birk, V. Boudon, L. R. Brown, A. Campargue, J. P. Champion, K. Chance, L. H. Coudert, V. Dana, V. M. Devi, S. Fally, J. M. Flaud, R. R. Gamache, A. Goldman, D. Jacquemart, I. Kleiner, N. Lacome, W. J. Lafferty, J. Y. Mandin, S. T. Massie, S. N. Mikhailenko, C. E. Miller, N. Moazzen-Ahmadi, O. V. Naumenko, A. V. Nikitin, J. Orphal, V. I. Perevalov, A. Perrin, A. Predoi-Cross, C. P. Rinsland, M. Rotger, M. Šimečková, M. A. H. Smith, K. Sung, S. A. Tashkun, J. Tennyson, R. A. Toth, A. C. Vandaele, and J. V. Auwera, “The HITRAN 2008 molecular spectroscopic database,” *Journal of Quantitative Spectroscopy & Radiative Transfer*, vol. 110, pp. 533–572, 2009.

[28] D. Pugh, J. Runyon, P. Bowen, A. Giles, A. Valera-Medina, R. Marsh, B. Goktepe, and S. Hewlett, “An investigation of ammonia primary flame combustor concepts for emissions reduction with OH*, NH_2* and NH* chemiluminescence at elevated conditions,” *Proc. Combust. Inst.*, vol. 38, pp. 6451–6459, 2021.

[29] “Holthuis and Associates flat flame burner, The calibration standard for combustion studies,” Flatflame, 6 March 2023, https://www.flatflame.com/.

APPENDIX A

PILOTED NH_3-BLEND FLAME STARTUP, OPERATION, AND SHUTDOWN PROCESSES

To Start Up:

1. Ensure mass flow controllers are closed, **water coolant is flowing**, and burner cover is removed.
2. Set each mass flow controller's flow rates for startup:
    a. Pilot channel H_2: 1 SLM
    b. Pilot channel air: 1 SLM
    c. Main channel H_2: 1.46 SLM
    d. Main channel NH_3: 1.30 SLM
    e. Main channel N_2: 0.486 SLM
    f. Main channel air: 3.5 – 4 SLM
3. Open all gas's cylinder valves, set regulator dials to 40 psi (pressure losses after mass flow controllers will yield atmospheric pressure flames).
4. Turn on NH_3 detector.
5. Turn on main flame mass flow controllers:
    a. Main channel air
    b. Main channel H_2
    c. Main channel N_2
    d. Main channel NH_3
6. Use lighter to start the main flame.
7. Slowly increase main air flow rate until intended equivalence ratio is reached, typically 1.35.

NOTE: under ~ 1.35 equivalence ratio has typically needed pilot flame to not blow out.

Introducing Low-Flow-Rate Pilot Flame:

1. Turn on pilot channel H_2 and air.
2. Slowly increase pilot air and pilot H_2 flow rate to intended values, usually H_2-2.0 SLM and air-4.76 SLM for the low-flow-rate pilot.

   NOTE: Alternate which species is being increased to avoid the pilot going excessively lean or rich, as flashback or blowout of the pilot may be a concern.

Further decreasing Equivalence ratio:

1. Slowly increase main flame air flow rate, especially once reaching stability limits around equivalence ratios of ~ 0.7.

Introducing High-Flow-Rate Pilot Flame:

1. Slowly increase pilot air and H_2 flow rates to 9.52 SLM and 4.0 SLM respectively.

Further decreasing Equivalence ratio:

1. Very slowly increase main flame air flow rate. Increasing too quickly could cause blow out at excessively lean conditions.

To Shut down:

1. If at lean equivalence ratios, shut off the pilot H_2 and air channels to cause blow out (no risks associated, **much safer than risking flashback** when burning at rich conditions).
2. If at rich or stoichiometric equivalence ratios, it is suggested to increase the air flow rate of the main flame to reach lean conditions and initiate blow out as in shut down step 1.
3. Turn off main flame NH_3, H_2, N_2, and air channels.
4. Turn off coolant water flow.

Cylinder shut off process:

1. Close all gas's cylinder dials, do not yet close regulator dial pressures.
2. Open all mass flow controller channels to allow remaining gas in pipes to purge.
3. Channel flow rates on controller display will turn red when that respective channel's gas flow rates are negligible (i.e. the pipe is purged).
4. Once both pilot and main H_2 channels report negligible flow rates, close H_2 regulator dial.
5. Once both pilot and main air channels report negligible flow rates, close air regulator dial.
6. Once NH_3 and N_2 channels report negligible flow rates, close NH_3 and N_2 regulator dials.

   NOTE: N_2 channel usually takes the longest to purge given its extremely low flow rate.